

# Impact of Radiometric Variability on Ultra-High Resolution Hyperspectral Imagery Over Aquatic Vegetation: Preliminary Results

Erika Piaser <sup>1</sup>, Andrea Berton, Rossano Bolpagni <sup>2</sup>, Michele Caccia <sup>3</sup>, Maria Beatrice Castellani <sup>4</sup>,  
Andrea Coppi <sup>5</sup>, Alice Dalla Vecchia, Francesca Gallivanone, Giovanna Sona, and Paolo Villa <sup>6</sup>

**Abstract**—Over the last two decades, advancements in airborne imaging spectroscopy have prompted the exploitation of lightweight drones for detailed vegetation assessment at unprecedented resolutions. Yet, surface reflectance anisotropy and view-illumination effects may bias spectra extracted from push-broom scanners and derived spectral indices (SIs), particularly over aquatic vegetation, thus impacting the retrieval of biophysical and biochemical vegetation parameters. In this study, the impact of illumination conditions (overcast versus clear sky) and angular configurations (i.e., solar and viewing angles) on radiometric variability of centimetric resolution drone data was empirically investigated over four different aquatic plant species, representing different growth forms and canopy structures. Nadir-normalized reflectance spectra, broadband SIs, and the spectral angle distance to proximal leaf reflectance were used for characterizing and quantifying radiometric variability at canopy and leaf levels. Our findings demonstrated a decrement in reflectance under diffuse light conditions, especially in highly reflective domains within Green (520–580 nm) and Near-Infrared (700–850 nm) ranges, and a marked angular reflectance anisotropy in high absorption spectral

regions (i.e., 450–500 nm and 630–700 nm) for aquatic vegetation. The normalized difference vegetation index (NDVI) showed overall lower sensitivity to incoming light variability and angular configurations compared to other tested SIs, whereas the water adjusted vegetation index (WAVI), suitably designed for aquatic vegetation, was less affected by angular anisotropy in floating plants. Indeed, radiometric variability exhibited a dependence on aquatic plant features, i.e., leaf orientation, canopy structure, and affinity with water (as canopy background).

**Index Terms**—Drones, illumination conditions, imaging spectroscopy, push-broom sensor, reflectance anisotropy, wetlands.

## I. INTRODUCTION

THE need for wetlands conservation in face of the current biodiversity crisis has emphasized the importance of monitoring aquatic vegetation as a key component of these sensitive ecosystems [1], [2]. Remote sensing solutions have demonstrated good efficiency for assessing ecosystem status and changes, extremely sought for capabilities when dealing with wetland applications, due to limited accessibility and difficulties in carrying out comprehensive in situ data collection [3], especially over relatively large areas. Relevant applications have focused on retrieving aquatic vegetation cover type, canopy density, plant biomass, and stress [3], [4], [5]. Over the last two decades, imaging spectroscopy data and techniques (also known as hyperspectral) have been increasingly exploited for estimating and mapping vegetation parameters (biophysical and biochemical), thanks to implicit advantages and enhanced performance compared to multispectral optical data. In fact, hyperspectral data cover hundreds of narrow (< 10 nm), contiguous spectral bands covering the visible (VIS, 400–700 nm), near-infrared (NIR, 700–1000 nm) to short-wave infrared (SWIR, 1000–2500 nm) portions of the electromagnetic spectrum. Even if the literature on this topic is mostly based on terrestrial plants and crops [6], [7], [8], the potential of hyperspectral remote sensing extends to applications on aquatic vegetation, and few works from proximal and airborne platforms have been published over the last years (e.g., [9], [10], [11]). Spatial and spectral resolution limitations of satellite imagery and logistical and resources constraints imposed by airborne hyperspectral surveys have prompted the use of lightweight drones, or unmanned aerial vehicle (UAV). UAV features—in terms of affordability, operational flexibility, and high spatial resolution achievable

Manuscript received 1 February 2023; revised 8 April 2023, 30 May 2023, and 1 June 2023; accepted 1 June 2023. Date of publication 7 June 2023; date of current version 10 July 2023. This work was supported by the Project “macroDIVERSITY,” founded by the Ministry of Education, University and Research, PRIN 2017, under Grant 2017CTH94H. The work of A. Dalla Vecchia was benefited from the equipment and framework of the COMP-HUB Initiative and was supported by the “Departments of Excellence” program of the Italian Ministry for Education, University and Research (MIUR, 2018–2022). (Corresponding author: Erika Piaser.)

Erika Piaser and Paolo Villa are with the Institute for Electromagnetic Sensing of the Environment, National Research Council (IREA-CNR), 20133 Milan, Italy (e-mail: piaser.e@irea.cnr.it; villa.p@irea.cnr.it).

Giovanna Sona is with the Department of Civil and Environmental Engineering, Politecnico di Milano, 20133 Milan, Italy (e-mail: giovanna.sona@polimi.it).

Andrea Berton is with the Institute of Geosciences and Earth Resources, National Research Council (IGG-CNR), 56124 Pisa, Italy (e-mail: andrea.berton@cnr.it).

Rossano Bolpagni and Alice Dalla Vecchia are with the Department of Chemistry, Life Sciences and Environmental Sustainability, University of Parma, 43121 Parma, Italy, and also with the IREA-CNR, 20133 Milan, Italy (e-mail: rossano.bolpagni@unipr.it; alice.dallavecchia@unipr.it).

Michele Caccia and Francesca Gallivanone are with the Institute of Molecular Bioimaging and Physiology, National Research Council (IBFM-CNR), 20133 Milan, Italy, and also with the National Biodiversity Future Center, 90123 Palermo, Italy (e-mail: michele.caccia@gmail.com; francesca.gallivanone@ibfm.cnr.it).

Maria Beatrice Castellani and Andrea Coppi are with the Department of Biology, University of Florence, 50121 Firenze, Italy (e-mail: mariabeatrice.castellani@unifi.it; andrea.coppi@unifi.it).

This article has supplementary downloadable material available at <https://doi.org/10.1109/JSTARS.2023.3283773>, provided by the authors.

Digital Object Identifier 10.1109/JSTARS.2023.3283773

[12], [13]—well fit the needs for detailed mapping and monitoring of aquatic vegetation in complex wetland environments. In addition to challenges due to environmental setting, remote sensing applications to vegetation need to take into account the three-dimensional structural complexity of plant targets, in particular, when high-resolution data are used. In fact, canopy elements and arrangement, substrate type and characteristics (especially for aquatic plants), as well as solar and view direction significantly affect the amount and spectra of light received and reflected within the sensor field of view (FOV) [14]. Scanning instruments, such as push-broom cameras, are particularly prone to these effects depending on their across-track aperture, especially at the FOV extremes [15].

Reflected radiance measured from proximal or remote sensors is not only determined by target type and biophysical features but also influenced by distortion factors, such as illumination conditions (e.g., direct and diffuse radiation balance) and different angular configurations due to sun-target-sensor arrangement. These distortions are generally quantified through the bidirectional reflectance distribution function (BRDF; [16]). In vegetation, deviations from angular reflectance isotropy (i.e., Lambertian case) are mainly driven by structure, architecture (including shadow fraction), and optical properties of canopy elements [17], [18]. Radiometric variability and uncertainties in retrieved reflectance spectra and/or derived spectral indices (SIs) can lead to considerable biases in vegetation biophysical and biochemical parameters modeled from optical remote sensing data. In early works, vegetation BRDF and anisotropy were characterized via multiangular measurements made with goniometers in laboratory, or in situ, and under controlled [19], [20] or natural illumination conditions [21], [22]. Over the last decades, the increased availability of airborne and lightweight drone platforms and the increasing potential of sensor technologies, especially for hyperspectral data, laid the foundations for large-scale and empirical studies exploring the sensitivity of canopy reflectance to variability in angular configuration [23], [24], [25], [26], [27] and illumination condition [14], [28], [29], mainly focusing on terrestrial vegetation (including crops). This is not the case for aquatic vegetation: even if some authors have demonstrated the ineffectiveness of applications based on terrestrial vegetation over aquatic canopies [30], only few works have characterized the effect on aquatic plant reflectance exerted by illumination conditions [31] and angular configurations [32]. In fact, peculiar structural and canopy features of aquatic plants differentiate them from terrestrial vegetation, e.g., the presence of water in the canopy background (for floating and emergent plants) or foreground (for submerged plants), or different mechanisms driving the interaction with incident light compared to typical soil background of terrestrial canopies. Vanderbilt et al. [31] observed a specular reflectance peak in forward direction along the solar principal plane (forward hotspot) for inundated canopies, distinct from that typically found for terrestrial vegetation in backward direction, mainly due to shadow-hiding effects (backward hotspot; [21], [33]). Although under a simplified agronomical setting, Ishihara et al. [32] found minimal impacts of changing the ratio of diffuse to direct incoming light on SIs measured over paddy rice, which bears some similarities

to natural aquatic canopies. Empirical data and experimental investigations are more needed for advancing quantitative remote sensing applications targeting aquatic vegetation parameters as physical models simulating the interaction between aquatic canopy and water with the incident radiation are not mature yet. To our knowledge, the only comprehensive model is the Aquatic Vegetation Radiative Transfer model (AVRT) [34], but it has not been validated with data covering typical aquatic vegetation canopy heterogeneity.

Therefore, as radiometric variability of aquatic vegetation reflectance extracted from hyperspectral images can result into significant biases in the estimation of biophysical and biochemical parameters, targeted studies based on empirical data are needed, especially focusing on ultra-high-resolution imagery. This kind of data can in fact capture fine-scale features of plant diversity, spanning from canopy elements (e.g., flowers, stems) up to individual leaves. Such features cannot be observed in metric resolution, commonly achievable with hyperspectral cameras mounted on airplanes. Characterizing major radiometric variability is a prerequisite for attenuating potential biases connected to them, thus enhancing the quality of fine-scale applications of remote sensing in wetland ecosystems.

As a preliminary step into this topic, starting from the literature on angular anisotropy of terrestrial vegetation [17], [21], [33] and based on AVRT model outputs relative to water affine species [34], this work aims to empirically investigate and quantify the radiometric variability of aquatic vegetation under different illumination conditions, i.e., comparing acquisitions made under overcast and clear sky, and different angular configurations, i.e., accounting for different solar and view angles (including the scan direction). The analysis was based on a heterogeneous empirical dataset, summarizing the complexity of wetland ecosystems where aquatic plants are found. We focused on four aquatic plant species, representing different growth forms, along a gradient of water affinity. The work was developed based on hyperspectral imaging data at centimetric resolution acquired on purpose over different lakes and wetland systems in Italy using a push-broom camera mounted on an airborne drone.

## II. MATERIALS

### A. Study Areas and Dominant Aquatic Vegetation Species

Empirical data were collected in five different shallow lakes and wetlands in northern and central Italy: Lake Pusiano (45°48' N, 9°16' E) and Lake Annone (45°48' N, 9°20' E), the Torbiere del Sebino wetland (45°38' N, 10°1' E), Mantua lakes system (45°10' N, 10°47' E), and Lake Massaciuccoli (43°50' N, 10°20' E). The study areas host abundant and diverse aquatic vegetation communities representing a wide range of growth habit, canopy structure, and functional types.

Four aquatic plant species dominating the study areas were selected as the main targets of interest representing different plant morphologies (see Fig. 1): common reed, a tall riparian helophyte (*Phragmites australis*); sacred lotus, a hydrophyte with large leaves emerging above the water (*Nelumbo nucifera*); yellow water lily, a medium rooted floating-leaved hydrophyte

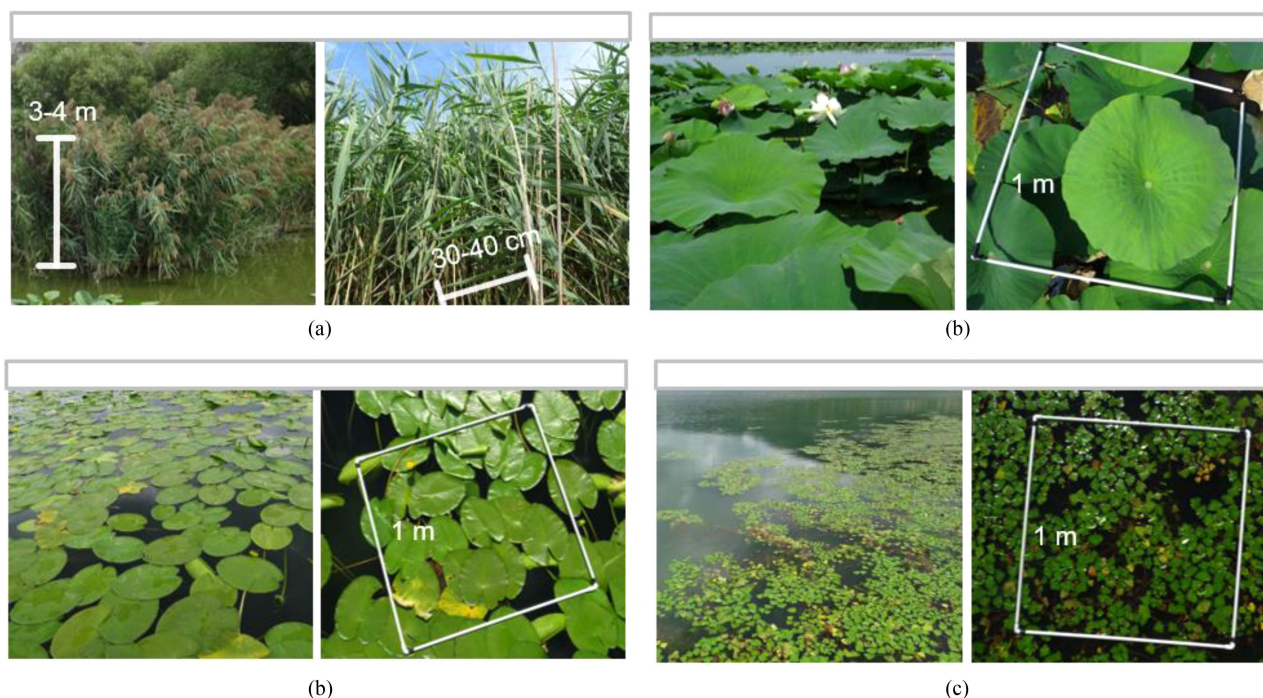


Fig. 1. Dominant aquatic vegetation species considered in this study within five shallow lakes and wetlands of interest: tall riparian helophytic emergent (a) *P. australis*, emergent (b) *N. nucifera*, floating with medium leaves (c) *N. lutea*, and floating and/or partially submerged (d) *T. natans* with small leaves.

(*Nuphar lutea*); and water chestnut, a small-leaved floating hydrophyte (*Trapa natans*). In the northern hemisphere at the study area latitudes, the plant growing season is usually between April and November for all the species.

*P. australis* [see Fig. 1(a)] is one of the most widespread flowering plants globally [35]. It is a riparian helophytic species, creating compact and often monospecific beds emerging for up to 3–4 m above water level [36], [37]. Each culm shows several boat-shaped, elongated (i.e., up to 40 cm long and 1–6 cm wide) leaves with gray-green color and flat, smooth sides.

*N. nucifera* [see Fig. 1(b)], original of south-eastern Asia, is a perennial herbaceous species with underwater rhizomes and leaves that can grow up to 1–2 m above the water [38]. The plant shows large and rounded (about 60–80 cm in diameter), regularly upward-cupped leaves of blue-green color. In our study sites, *N. nucifera* was introduced in 1920s and shows invasive habit, usually growing in high density stands (i.e., average leaf area index (LAI) up to 2; [39]).

*N. lutea* [see Fig. 1(c)] is a perennial herbaceous species native to temperate regions of Europe and Asia [40]. Its leaves have ovoidal shape, average diameter around 30 cm, and are floating and/or partially submerged, with light green color and a typical waxy texture. *N. lutea* canopies showed medium to high densities within our study sites (i.e., LAI between 0.6 and 1.2).

*T. natans* [see Fig. 1(d)] is an annual, weakly rooted plant with a wide native range, including the main temperate regions (i.e., between Europe, Africa, and Asia), and can show a habit toward expansiveness and even invasiveness around the globe [41]. It grows in slow-moving and shallow waters, shows small (i.e., 2–3 cm), triangular and strongly dentate dark green leaves,

arranged in rosettes floating on the water surface, occasionally forming dense floating mats.

The four selected species grow at different water depths, and water level ranges may vary depending on the site, the season, and climatic conditions.

### B. UAV Hyperspectral Data Acquisition

Hyperspectral images were acquired over target aquatic vegetation stands during the summer of 2021. Ultra-high, centimetric spatial resolution images were acquired over 32 vegetation plots with a hyperspectral push-broom camera (Nano-Hyperspec, Headwall Photonics, Bolton, Massachusetts), with a 22° FOV and 12 mm focal length, on 274 spectral bands in the Visible–Near-Infrared range (VNIR; 400–1000 nm) with 2.2 nm spectral resolution. The sensor was mounted on a multirotor UAV system composed by DJI M600 Pro drone and a Ronin MX 3-axis stabilizer (DJI, Shenzhen, China). The acquisition was set so that the sensor collected imagery along the flight direction line by line, with a swath width of 640 pixels, and a frame rate of 300 Hz. Flight height was set constant around 50 m altitude above the water level, resulting in 3 cm of pixel resolution on the ground (i.e., water).

Before each flight, optimal exposure was set depending on sunlight intensity by framing a white Spectralon polytetrafluoroethylene panel (nominal 99% reflectance) and connected flight velocity was set (4–5 m s<sup>-1</sup>).

Sensor dark current measurement was taken with a metal cap mounted on the camera lens and was used for image processing. During each flight, a reference image was captured framing a

TABLE I  
UAV SURVEYED PLOTS CHARACTERIZATION FOR RADIOMETRIC VARIABILITY ASSESSMENT DUE TO ILLUMINATION CONDITIONS

Plot ID <sup>a</sup>	Longitude	Latitude	Dominant species	Date	Local Time (UTC+2)	SZA (deg)	SAA (deg)	RAA (deg)	measured-simulated solar radiation (% VIS range)
IS23	10.035	45.641	<i>N. lutea</i>	10/09/2021	10:14:29	43.1	156.8	68.7	82
IS24	10.033	45.641	<i>N. lutea</i>	10/09/2021	10:09:33	43.5	155.0	37.9	82
MN33	10.687	45.178	<i>N. lutea</i>	29/07/2021	13:03:54	33.7	226.3	43.3	90
PA03	9.294	45.808	<i>N. lutea</i>	19/07/2021	10:45:02	26.6	156.4	58.3	94
IS26	10.032	45.647	<i>P. australis</i>	10/09/2021	09:27:09	47.3	141.3	43.1	69
IS27	10.031	45.646	<i>P. australis</i>	10/09/2021	10:50:39	41.3	170.2	70.6	53
MN19	10.697	45.157	<i>P. australis</i>	29/07/2021	13:50:18	40.3	240.9	35.2	90
PA25	9.357	45.809	<i>P. australis</i>	20/07/2021	13:56:55	39.4	242.6	61.3	98

For each plot, geographic coordinates, dominant species, surveying date, and time are reported as well as SZA, SAA, RAA, and measured-simulated solar radiation for clear sky (described in Section II C).

<sup>a</sup> IS=Torbriere del Sebino wetland; MN= Mantua lakes system; PA= Lakes Pusiano and Annone

3×3 m panel with three calibrated reflectance levels (i.e., 11%, 33%, 52%) positioned over a flat nonshadowed area to convert raw data to reflectance. UAV system attitude (i.e., longitude and latitude coordinates, roll, pitch, and heading angles) was recorded by camera Inertial Measuring Unit (IMU-GPS; frequency: 1000 Hz), with nominal positional accuracy of 2 m and angle nominal ratings lower than 0.3°.

### C. Surveyed Plot Characterization

A first batch of tests for assessing radiometric variability due to different illumination conditions (i.e., diffuse/direct light ratio) were conducted by comparing information derived from plots surveyed in overcast (Torbriere del Sebino) and clear sky (Mantua, Pusiano-Annone) conditions. Table I lists UAV surveys performed for this test, reporting the percentage of measured-simulated solar radiation ratio in the visible spectrum range (VIS: 400–700 nm). Simulated clear sky solar irradiance on the ground was calculated with the Bird simple spectral model [42]. Further tests, aimed at assessing radiometric variability due to sun-target-sensor angular configuration, were conducted in clear sky conditions, with no wind and stable light intensity, and reported in Table II.

For each of the 32 aquatic vegetation surveyed plots, Tables I and II report flight specific features (i.e., site location, surveyed species, flight date, and local time), and solar position in terms of both sun zenith angle (SZA), sun azimuth angle (SAA) and relative azimuth angle (RAA). The mentioned quantities define solar elevation, solar principal plane direction, and the absolute value of angular distance between SAA and the sensor scan direction, respectively. Table II also reports the additional information on angular configuration category (Zone ID, described in Supplementary Material, Table SI), based on SZA and RAA combinations. SZA and RAA thresholds, set for discriminating plots within different zones, were established according to the AVRT model [34], from simulations of reflectance anisotropy across three different zenith angles (i.e., 30°, 45°, and 60°), both for solar principal (PP) and orthogonal (OP) planes. Based on this, we categorized Zone ID considering 30° as a threshold for SZA, and 30° and 60° as thresholds for RAA. Plots with a scan direction approximately parallel to the solar PP (0° < RAA

< 30°) and relatively high or moderate sun elevation (SZA < 30° or ≥ 30°, respectively) are classified within Zone A and B, respectively. In these zones, radiometric anisotropy due to vegetation hotspot and background effects can be expected. Plots with intermediate RAA angular configurations (30° < RAA < 60°) are delineated as Zone C, where anisotropy risk is mainly depending on the type of vegetation target (canopy structure and background). Finally, plots with scan direction approximately perpendicular to the solar PP (60° < RAA < 90°) and SZA < 30° or ≥ 30° are classified within Zones D and E, respectively. Plots within Zone D are expected to present anisotropy risk if the dominant effect is due to the SZA, whereas for Zone E, angular distortions are expected to be minimal.

Plots used for assessing the impact of variable sun-target-sensor angular configurations on derived radiometry (see Table II) were further clustered into two macrogroups—i.e., “Favorable” and “Non-favourable” angular configurations—according to the dominance of SZA and/or RAA in determining reflectance anisotropy risk for each of four target species and based on dominant canopy architecture and structure (see Supplementary Material, Figs. S1 and S2). For species with leaves emerging above water (i.e., *N. nucifera* and *P. australis*), categories were separated based on Zone ID—i.e., Zones C, D, and E were labeled as Favorable, and Zones A and B were labeled as Non-favourable. For species with leaves floating on or very near to the water surface (i.e., *N. lutea* and *T. natans*), the subdivision was based on SZA as the dominant factor of anisotropy risk—i.e., plots with SZA ≥ 30° were labeled as Favorable, and those with SZA < 30° were labeled as Non-favourable.

### D. Auxiliary Field Data Measurements

In situ hyperspectral leaf reflectance was acquired during boat-based surveys carried out some days before UAV flights (i.e., from 2 to 10 days in advance, for Torbriere del Sebino and Mantua lakes system, respectively) with a full-range portable spectroradiometer (SR-3500, Spectral evolution, Haverhill, Massachusetts) equipped with an active contact probe. The spectral range of the instrument is 350–2500 nm with a spectral resolution of 2.8 nm in the VNIR (i.e., up to 1000 nm) and 6–8 nm in the SWIR (1000–1500 nm). Leaf reflectance of

TABLE II  
UAV SURVEYED PLOTS CHARACTERIZATION FOR RADIOMETRIC VARIABILITY ASSESSMENT DUE TO SUN-TARGET-SENSOR ANGULAR CONFIGURATIONS

Plot ID <sup>a</sup>	Longitude	Latitude	Dominant species	Date	Local Time (UTC+2)	SZA (deg)	SAA (deg)	RAA (deg)	Zone ID
MN28	10.813	45.135	<i>T. natans</i>	30/07/2021	10:12:13	30.6	145.2	62.1	E
PA02	9.294	45.807	<i>T. natans</i>	19/07/2021	10:44:34	26.7	156.0	21.4	A
PA10	9.255	45.794	<i>T. natans</i>	19/07/2021	9:47:00	32.6	131.5	85.3	E
PA13	9.254	45.792	<i>T. natans</i>	19/07/2021	9:46:20	32.7	131.3	41.3	C
PA18	9.327	45.811	<i>T. natans</i>	20/07/2021	11:38:00	25.3	184.9	66.7	A
PA20	9.340	45.815	<i>T. natans</i>	20/07/2021	11:41:57	25.4	187.1	7.8	D
PA24	9.357	45.807	<i>T. natans</i>	20/07/2021	13:57:55	39.5	242.9	7.0	B
MN05	10.726	45.162	<i>N. nucifera</i>	29/07/2021	10:40:05	28.0	157.6	64.3	D
MN08	10.740	45.159	<i>N. nucifera</i>	30/07/2021	09:00:46	39.9	120.4	17.0	B
MN18	10.697	45.158	<i>N. nucifera</i>	29/07/2021	14:01:11	42.0	243.8	27.0	B
MN35	10.690	45.177	<i>N. nucifera</i>	29/07/2021	13:01:56	33.5	225.6	43.3	C
MA01	10.337	43.850	<i>P. australis</i>	02/07/2021	12:27:52	24.8	218.0	4.6	A
MA07	10.352	43.844	<i>P. australis</i>	01/07/2021	14:58:17	20.9	175.7	87.1	D
MA08	10.327	43.858	<i>P. australis</i>	02/07/2021	12:46:20	27.0	226.1	3.2	A
MA16	10.340	43.824	<i>P. australis</i>	01/07/2021	15:01:10	49.0	263.4	71.5	E
MN09	10.734	45.160	<i>P. australis</i>	29/07/2021	10:44:13	27.8	159.6	65.3	D
MN12	10.709	45.158	<i>P. australis</i>	29/07/2021	13:56:38	41.4	242.8	28.4	B
MN15	10.698	45.162	<i>P. australis</i>	29/07/2021	13:59:53	41.8	243.6	28.0	B
PA04	9.291	45.809	<i>P. australis</i>	19/07/2021	10:46:94	26.6	156.9	39.0	C
PA06	9.291	45.810	<i>P. australis</i>	19/07/2021	10:46:56	26.5	157.4	86.7	D
PA19	9.333	45.812	<i>P. australis</i>	20/07/2021	11:36:35	25.3	183.8	23.8	A
MN13	10.705	45.158	<i>N. lutea</i>	29/07/2021	13:55:11	41.1	242.3	23.2	B
MN24	10.820	45.135	<i>N. lutea</i>	30/07/2021	10:16:26	30.2	146.9	85.4	E
MN27	10.816	45.137	<i>N. lutea</i>	30/07/2021	10:14:47	30.3	146.5	64.1	E
MN33	10.687	45.178	<i>N. lutea</i>	29/07/2021	13:03:54	33.7	226.3	43.3	C
PA03	9.294	45.808	<i>N. lutea</i>	19/07/2021	10:45:02	26.6	156.4	58.3	C

For each plot, geographic coordinates, dominant species, surveying date, and time are reported as well as SZA, SAA, RAA, and Zone ID based on SZA and RAA combinations (described in Supplementary Material).

<sup>a</sup> IS=Torbiere del Sebino wetland; MN= Mantua lakes system; PA= Lakes Pusiano and Annone; MA=Lake Massaciuccoli

the dominant species of each surveyed plot (see Tables I and II) was measured for eight leaves (after cleaning and drying with a soft tissue) and averaged per plot.

### III. METHODS

#### A. Hyperspectral Data Processing

UAV hyperspectral data were processed with Headwall SpectralView - Hyperspec v.3.1.5.1 software to derive georeferenced reflectance images from raw data. In this study, the bidirectional reflectance factor extracted from hyperspectral image pixels, henceforth referred to simply as reflectance ( $R$ ), is derived as

$$R(SZA, RAA, VZA, \lambda) = \frac{L_r(SZA, RAA, VZA, \lambda)}{L_r^{p52}(SZA, RAA, VZA, \lambda)} RF^{p52}(\lambda) \quad (1)$$

as function of sun and viewing zenith angles (SZA and VZA, respectively), the angular distance between sun azimuth and sensor's scan azimuth (RAA), and wavelength ( $\lambda$ ), where  $L_r$  and  $L_r^{p52}$  are the radiance reflected respectively from a target pixel and from a reference bright calibration panel, with known absolute reflectivity factor  $RF^{p52}(\lambda)$  (52% average in 400–1000 nm range).

The calibration panel and target aquatic vegetation plots are surveyed during the same flight, i.e., under stable illumination conditions. SZA and RAA of target plots are reported in Tables I and II, while VZA is represented by three across-track viewing angle ranges (see Section II-B). Reflected radiance was obtained by the radiometric calibration of Nano-Hyperspec sensor data.  $L_r$  ( $\text{mW cm}^{-2} \text{sr}^{-1} \mu\text{m}^{-1}$ ) was derived for each pixel in the images containing aquatic vegetation plots, while  $L_r^{p52}$  ( $\text{mW cm}^{-2} \text{sr}^{-1} \mu\text{m}^{-1}$ ) was computed averaging the reflected radiance of manually selected pixels falling within the nadiral portion of the calibrated reference panel on hyperspectral images.

Due to the lack of a digital surface model (DSM) with an adequate resolution, images were georeferenced by orthorectification on a plane with constant elevation (i.e., a distance of 50 m from the sensor). This georeferencing is performed by applying a direct photogrammetry approach based on information provided by IMU/GPS data (i.e., camera position and attitude angles), relative to each scan line. Since the sensor is of a push-broom type, it acquired a single swipe over each surveyed plot, thus obtaining a total of 32 hyperspectral georeferenced data cubes, characterized by 274 spectral bands, with around 3 cm spatial and 2 nm spectral resolutions. Postprocessing of the georeferenced data cubes was performed via the Environment for Visualizing Images (ENVI; v. 5.6.2) software application, including: 1) spatial subset around

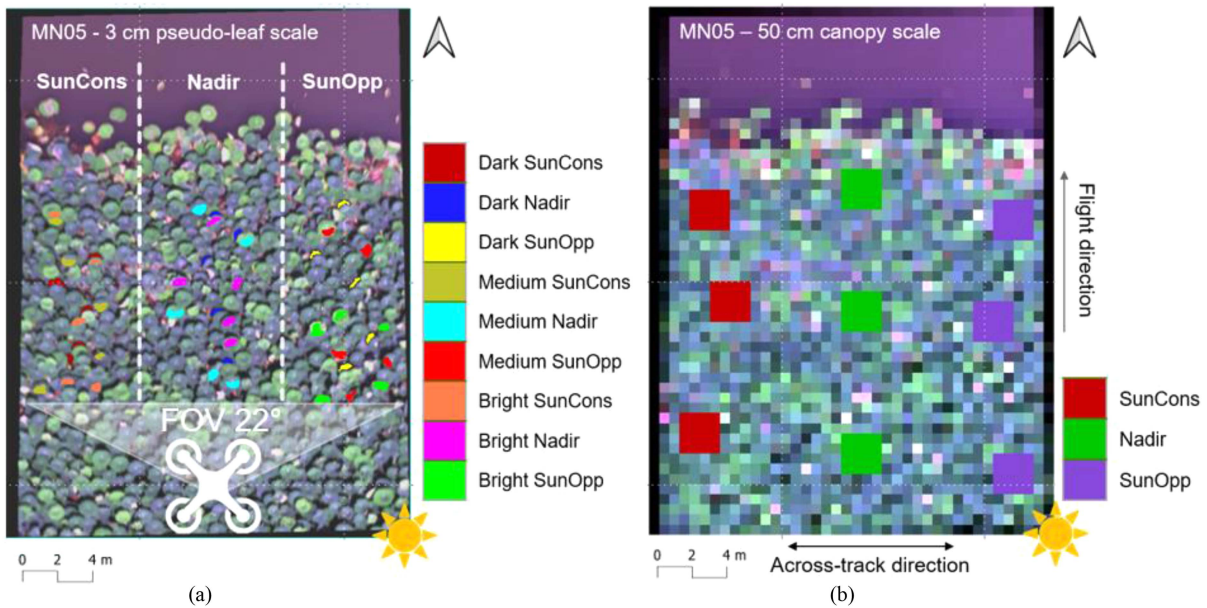


Fig. 2. Example of (a) pseudo-leaf ROIs within three different levels of brightness: dark, medium, and bright. (b) Canopy level ROIs, delineated over 3 cm and resampled 50 cm spatial resolution hyperspectral imagery, for sacred lotus plot MN05 (*N. nucifera*). ROIs were outlined within off-nadir lateral zones within consistent (i.e., SunCons) and opposite (i.e., SunOpp) viewing angle with respect to the sun beam direction, respectively, and within the central nadiral zone (i.e., Nadir).

the area of interest of in situ acquired measurements; 2) spectral smoothing via Savitzky–Golay filter [43]; and 3) conversion to cartographic projection UTM 32N (WGS84 datum).

Moreover, a resampled version of each hyperspectral cube to 50 cm spatial resolution was produced to explore the radiometric variability at a different scale.

### B. Region of Interest (ROI) Delineation

To explore how sun-target-sensor geometry affects reflectance values, ROIs were delineated over each plot at two different scales (or levels of detail): leaf and canopy. Due to the size and regular geometry of *N. nucifera* leaves, ROIs at leaf scale for this species represent a portion of the adaxial leaf side. Homologous ROIs for the other species do not exactly represent leaf reflectance due to comparable or small leaf size respect to the image resolution (*T. natans*, *P. australis*), variability in leaf orientation (*P. australis*), and presence of various nonphotosynthetic materials above the leaves (epiphytes, sediment, water film; *N. lutea*, *T. natans*). For this reason, in the rest of this work, such ROIs are more properly referred to as pseudo-leaf scale. ROIs at canopy scale contain different plant parts (e.g., inflorescences, stems, litter material) and leaves with multiple orientations, as well as some water background visible through canopy gaps, which are all factors that interact with the incident light influencing the canopy reflectance as measured from remote imagery.

Each processed cube was divided into three VZA zones of approximately the same width along the across-track direction: the central zone, located in the center of the data strip (absolute view angle  $\leq 3.6^\circ$  from nadir), and two lateral zones covering off-nadir angles  $> 3.6^\circ$  (and up to  $11^\circ$ ) in both scan directions. By considering the solar position during each flight, one lateral

zone is seen by the sensor under a view angle consistent with the incident solar beam direction and defined as “SunCons” zone. The other zone, seen under a view angle opposite to that of the sun, is defined as “SunOpp” zone. With respect to the solar PP, SunOpp direction is when the sensor view tends toward the sun and could also be referred as forward direction, whereas SunCons represents a configuration with sensor view angle in backward direction. Fig. 2 shows a graphical example of this approach over an *N. nucifera* plot in the Mantua lakes system site (MN05) for both pseudo-leaf [see Fig. 2(a)] and canopy scale ROIs [see Fig. 2(b)].

Pseudo-leaf ROIs were delineated within each zone (i.e., SunOpp, Nadir, and SunCons) by photointerpretation of 3 cm spatial resolution images in ENVI software, accounting for three levels of leaf brightness (i.e., dark, medium, and bright [see Fig. 2(a)] based on VNIR albedo. Dark ROIs correspond to shaded areas for species with emergent leaves (*N. nucifera* and *P. australis*) or to senescing or partially wet leaves for floating species (*N. lutea* and *T. natans*). Bright ROIs represent highly reflective green areas, mainly due to specular reflection combining leaf orientation and sun angle for all species. Medium ROIs show intermediate leaf brightness, representing a spectral response more like healthy, mature leaves, on average. Canopy level ROIs in Fig. 2(b) were manually delineated over 50 cm resampled data by considering square polygons with 1 m side, reaching 2 m side for homogeneous canopies of broad-leaved *N. nucifera* stands.

### C. Assessment of Radiometric Variability

The assessment of radiometric variability derived from centimetric resolution hyperspectral push-broom data over different aquatic vegetation types was performed considering two

different sources of distortion: illumination conditions (see Table I), and angular configurations (see Table II). Toward this, three metrics were used for characterizing different ROIs: 1) pseudo-leaf and canopy spectra, in terms of absolute reflectance and nadir-normalized reflectance; 2) broadband SIs at canopy scale; 3) spectral similarity between reflectance extracted from hypercubes and acquired at leaf contact.

In order to assess radiometric variability over aquatic vegetation stands due to illumination conditions (i.e., clear versus overcast sky), pseudo-leaf and canopy spectral profiles of plots listed in Table I were compared in pairs: those that surveyed under partially or totally overcast sky conditions (i.e., IS23, IS24, IS26, and IS27 in Torbiere del Sebino wetland), and those that surveyed under clear sky conditions (i.e., MN33, PA03, MN19, and PA25). The differences between ROI reflectance (at pseudo-leaf and canopy scales) acquired under overcast and clear sky conditions were evaluated—separately for SunCons, Nadir, and SunOpp across-track zones—for *N.lutea* and *P. australis* as they are the only species present in Torbiere del Sebino wetland site.

The impact of radiometric variability due to varying angular configurations (i.e., SZA and RAA combination) was assessed by deriving nadir-normalized reflectance spectra over plots listed in Table II. Broadly used in previous literature [23], [24], [44], this approach provides a straightforward way to characterize key spectral anisotropy features in vegetation.

Within our simplified experimental design, the derived nadir-normalized reflectance, or anisotropy factor (ANIF), was computed via (2) [44] for off-nadir directions (i.e., SunOpp and SunCons, respectively, assimilable to forward and backward views in the solar PP) as the ratio between the reflectance extracted from off-nadir zones over the average reflectance extracted from the nadir zone:

$$\text{ANIF}(\text{SZA}, \text{RAA}, \lambda) = \frac{R(\text{SZA}, \text{RAA}, \lambda)_{\text{Off-nadir}}}{R(\text{SZA}, \text{RAA}, \lambda)_{\text{Nadir}}} \quad (2)$$

where  $R_{\text{Nadir}}$  is the average reflectance extracted from ROIs in the central nadir zone, and  $R_{\text{Off-nadir}}$  is the reflectance extracted from ROI pixels falling within off-nadir zones (i.e., SunOpp or SunCons) at specific wavelength  $\lambda$  (400–1000 nm) and function of solar and viewing angles. The closer the ANIF is to unit value, the lower the impact of radiometric anisotropy in the off-nadir viewing direction. The assessment of the main physical factors affecting radiometric variability takes into account the vegetated canopy and the water surface as main contributors to reflectance anisotropy of the canopy-background system in aquatic vegetation, while angular variability in water reflectance due to optically active particles in the water column is considered negligible.

In addition, four common SIs were examined in terms of absolute and nadir-normalized values computed from ROIs at canopy scale over all the aquatic vegetation target plots listed in Tables I and II. Table III reports the selected SIs and their underlying formulas. The normalized difference vegetation index (NDVI) is considered a proxy of the overall amount of photosynthetic material in canopies [45]. The enhanced vegetation index (EVI) was introduced by Huete [46] as an enhancement of NDVI,

TABLE III  
LIST OF SIS SELECTED IN THIS STUDY AND THEIR FORMULAS

SI	Formula
EVI	$G * (R_{\text{NIR}} - R_{\text{RED}}) / (R_{\text{NIR}} + C1 * R_{\text{RED}} - C2 * R_{\text{BLUE}} + L)$ <sup>a</sup>
NDVI	$(R_{\text{NIR}} - R_{\text{RED}}) / (R_{\text{NIR}} + R_{\text{RED}})$
TGI	$-0.5 * [(\lambda_{\text{RED}} - \lambda_{\text{BLUE}}) * (R_{\text{RED}} - R_{\text{GREEN}}) - (\lambda_{\text{RED}} - \lambda_{\text{GREEN}}) * (R_{\text{RED}} - R_{\text{BLUE}})]$ <sup>b</sup>
WAVI	$1.5 * (R_{\text{NIR}} - R_{\text{BLUE}}) / (R_{\text{NIR}} + R_{\text{BLUE}} + L)$ <sup>c</sup>

a. G=2, C1=6, C2=7.5, L=1  
b.  $\lambda$  is the central band wavelength  
c. L=0.5

accounting for atmospheric and vegetation background noise [47]. The triangular greenness index (TGI) is linked to the chlorophyll content of terrestrial vegetation [48]. As these SIs were designed for terrestrial vegetation applications, we added the water adjusted vegetation index (WAVI), which is sensitive to aquatic vegetation canopy density and biomass [49]. Being these SIs originally defined in the literature as broadband vegetation indices, using reflectance measured from multispectral instruments, each hypercube was first spectrally resampled in ENVI software to match Copernicus Sentinel-2 (S2) band resolution; then, the resulting S2 simulated bands were used for computing the target SIs. After this, mean and standard deviation of each SIs were extracted from ROIs at canopy scale, within SunCons, Nadir, and SunOpp viewing directions. Consequently, mean and standard deviation of nadir-normalized SIs were computed similarly to ANIF.

To further evaluate spectral variability over aquatic vegetation from UAV-based hyperspectral push-broom imagery, the spectral separability between image-derived pixel reflectance in near-nadir conditions and reference spectra acquired from the same vegetation was calculated using the spectral angle distance (SAD) metric via (3) [50]

$$\text{SAD} = \cos^{-1} \frac{\sum_{i=1}^n ID_i IS_i}{\sqrt{\sum_{i=1}^n ID_i^2} \sqrt{\sum_{i=1}^n IS_i^2}} \quad (3)$$

where SAD is measured in radians,  $ID_i$  is pseudo-leaf ROIs image-derived reflectance (medium brightness), and  $IS_i$  is the reference leaf spectra acquired at contact (in situ), across the  $n$  spectral bands.

To allow the comparison of the spectra, leaf reflectance measured at contact with the SR3500 portable spectroradiometer was fitted with a continuous function using spline interpolation (R package “prospectr”), and new spectra with the same band centers as the Nano-Hyperspec cubes were extracted from it. The higher is the SAD, the higher is the deviation of image-extracted reflectance spectra from leaf-level standardized measures.

## IV. RESULTS

### A. Impact of Illumination Condition on Reflectance Spectra

Fig. 3 shows the impact of illumination conditions in the range 400–850 nm (where signal noise is low) on plot-averaged spectral reflectance difference between overcast plots and their counterpart in clear sky conditions: results are relative to pseudo-leaf

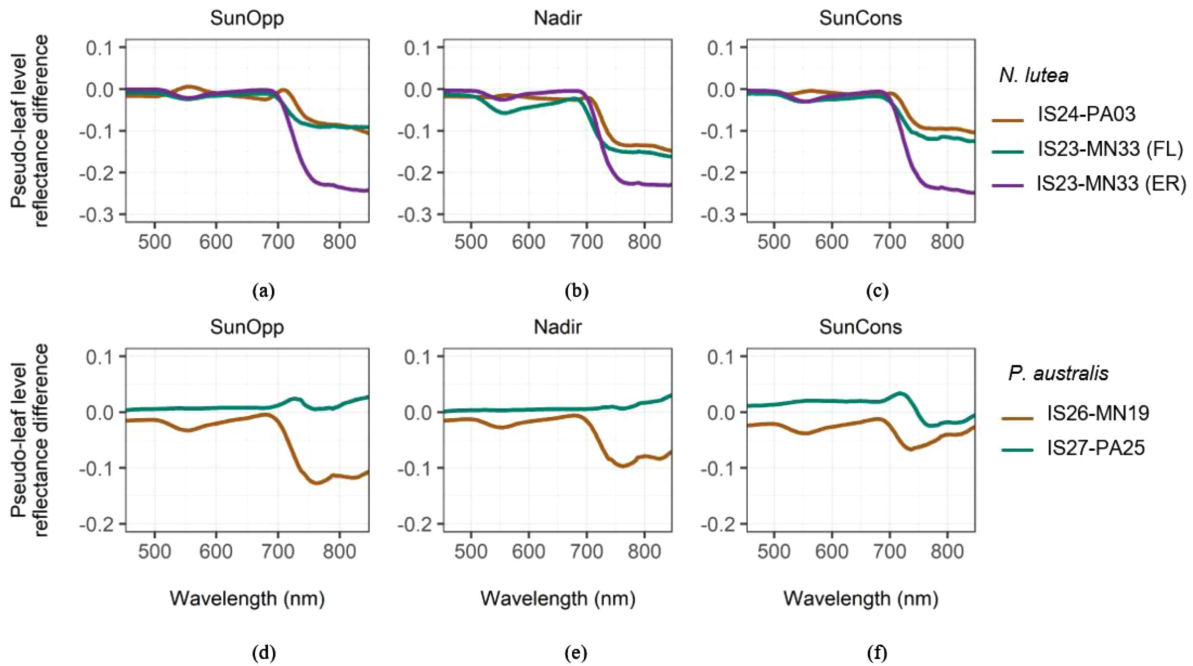


Fig. 3. Spectral reflectance curve differences at pseudo-leaf scale between surveyed plots under overcast (IS23–27) and clear sky for (a)–(c) floating *N. lutea* and (d)–(f) emergent *P. australis* aquatic vegetation stands within two off-nadir view ranges opposite (SunOpp) and consistent (SunCons) with the sun direction, and within nadir viewing direction (i.e., Nadir). For *N. lutea* IS23 and MN33 plots, both floating (FL) and emergent (ER) pseudo-leaf spectra are shown. For Plot ID codes, refer to Table I.

ROIs and distinctly cover SunOpp, Nadir, and SunCons viewing directions for floating and emergent *N. lutea* [see Fig. 3(a)–(c)] and *P. australis* [see Fig. 3(d)–(f)], respectively. The homologous representation at canopy scale is reported in Supplementary Materials (see Fig. S5). Overall, lower spectral reflectance is derived for both *N. lutea* and *P. australis* when plots are acquired in partially overcast sky conditions (diffuse illumination dominance), compared to clear sky conditions (direct illumination dominance). This difference tends to be approximately proportional to the absolute magnitude of target reflectance; as a result, spectral domains where vegetation reflects more of incoming light (i.e., NIR and Green) are more sensible to diffuse/direct light ratio than spectral ranges where vegetation reflectance is low (i.e., leaf-pigments absorbance regions in Red and Blue). This effect is consistent over all viewing directions (SunOpp, Nadir, and SunCons). Three pairs of ROIs were compared for *N. lutea*: IS24-PA03 with floating leaves and IS23-MN33 with both floating (FL) and emergent (ER) leaves (see Supplementary Material, Fig. S8). At pseudo-leaf level in Fig. 3(a)–(c), emergent leaves show a decrease in reflectance with overcast sky conditions (up to 0.25 in the NIR) more marked than floating leaves ROIs (up to 0.15 in the NIR). IS24-PA03 pair registered a slightly low decrease in reflectance than IS23-MN33 pair across the whole domain. The slight peak of reflectance difference in the Green range for IS24-PA03 pair is due to peculiar leaf color of *N. lutea* ROIs in IS24. Results obtained by the analysis at canopy level (see Supplementary Material, Fig. S5) are similar to those at pseudo-leaf level but slightly less marked in magnitude. Reflectance spectra at both pseudo-leaf and canopy level, within the three viewing directions, are reported in Supplementary Material (see Figs. S3, S4, S6, and S7, respectively).

The illumination condition effects on *P. australis* reflectance, presented in Fig. 3(d)–(f), tend to be similar to those of floating-leaved ROIs of *N. lutea* for what concerns the IS26-MN19 pair, while the behavior of IS27-PA25 pair is notably different. Indeed, the latter comparison is hampered by non homogeneous canopy density and ROIs displacement in SunOpp zone for *P. australis* stands in PA25 so that only SunCons zone can be considered consistent with corresponding ROIs in IS27. Over IS26-MN19 pair, NIR differences are more evident in SunOpp [up to 0.12, Fig. 3(d)] than in SunCons [up to 0.06, Fig. 3(f)] at pseudo-leaf scale, whereas differences are once again slightly attenuated at canopy level (see Supplementary Material, Fig. S5).

### B. Impact of Illumination Conditions on Spectral Indices

Fig. 4(a) reported the comparison of EVI, NDVI, TGI, and WAVI over plots with different illumination conditions for *N. lutea* by angular configuration. As a general pattern, plot surveyed under overcast sky conditions tend to score lower SI values than those under clear sky. EVI varies from 0.38–0.50 to 0.50–0.78, NDVI from 0.65–0.85 to 0.70–0.90, TGI from 3–6 to 4–8, and WAVI from 0.40–0.60 to 0.58–0.78, respectively, in plots surveyed under overcast sky and clear sky conditions.

Emergent leaves (IS23-MN33 pair) showed higher EVI, NDVI, and WAVI, and lower TGI values than floating leaves due to canopy optical properties (i.e., lower Green and higher NIR reflectance). Fig. 4(b) reports the same SIs comparison for *P. australis* plots. Again, SIs tend to score lower values in acquisitions made under overcast sky conditions. NDVI is the index that attenuates more the difference due to incoming light conditions

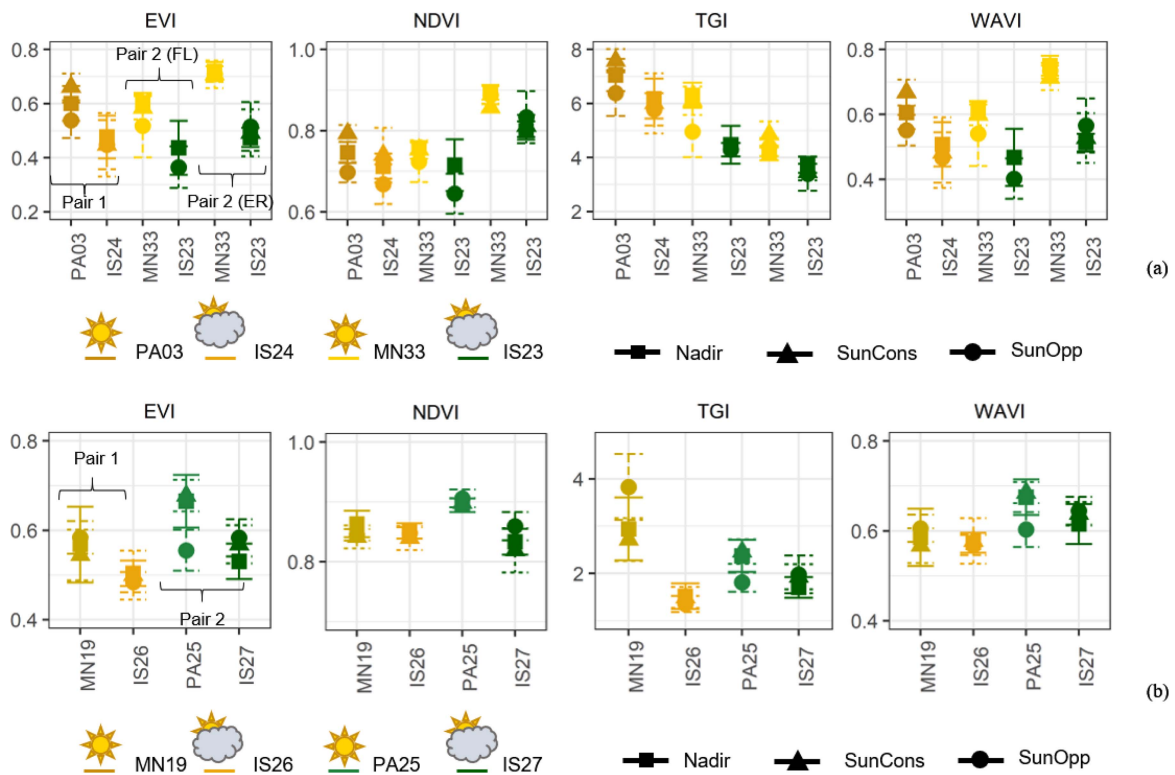


Fig. 4. Mean and standard deviation values for EVI, NDVI, TGI, and WABI from (a) floating *N. lutea* stands and (b) emergent *P. australis* stands, display as function of plot ID. In the legend, the yellow sun marks clear sky plots, while the gray cloud marks overcast sky plots (IS plots). Square, triangular, and circular symbols for each plot refer to Nadir, SunCons (consistent with the sun direction), and SunOpp (opposite to the sun direction) viewing direction, respectively. In panel (a), IS23 and MN33 for floating (FL) and emergent (ER) leaves are separated. For Plot ID codes, refer to Table I.

for IS26-MN19 pair (i.e., 0.85–0.86 under overcast and clear sky, respectively), while WABI scores lowest differences for IS27-PA25 pair (i.e., 0.65–0.70). EVI scores are 0.50–0.60 and 0.60–0.68, while TGI varies from 1.5–2 to 1.9–4, respectively, in plots surveyed with overcast sky and with clear sky conditions.

### C. Leaf Spectra Similarity Under Different Illumination Conditions

Fig. 5 reports SAD for *N. lutea* and *P. australis* plots listed in Table I. Plots surveyed under overcast sky show average SAD values higher than the clear sky homologues for both floating-leaved *N. lutea* and tall helophyte *P. australis*. For *N. lutea*, floating pseudo-leaf ROIs in MN33 (clear sky) scored similar SAD to IS23 (overcast sky) because average leaf spectra measured at contact were biased toward those of emergent leaves dominant in this plot.

The radiometric variability induced by different illumination conditions is less visible in emergent (SAD = 0.054–0.053, under overcast and clear sky, respectively) than floating *N. lutea* leaves. *P. australis* overcast plots score SAD around 0.16, compared to 0.12–0.14 over plots acquired in clear sky conditions.

### D. Impact of Angular Configurations on Reflectance Spectra

Mean and standard deviation of ANIF at pseudo-leaf level in SunOpp and SunCons directions (400–850 nm), covering three different brightness levels (i.e., Dark, Medium, and Bright

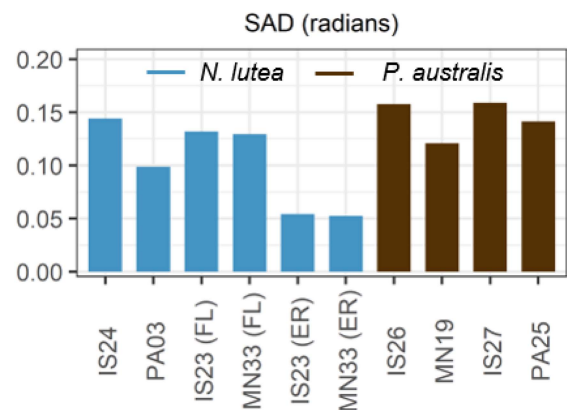


Fig. 5. Spectral similarity evaluation with SAD metric between reference in situ spectra and image-based nadiral pseudo-leaf spectra extracted from hyperspectral cubes for *N. lutea* and *P. australis* aquatic vegetation plots varying illumination conditions. For *N. lutea* IS23 and MN33, plots separately show floating (FL) and emergent (ER) leaves. For Plot ID codes, refer to Table I.

leaves), are shown in Fig. 6 for Non-favourable angular configurations. Aquatic vegetation reflectance variability due to sun-target-sensor arrangement shows strong wavelength dependence, especially in the VIS domain, with Blue and Red ranges as the most influenced by spectral anisotropic effects. Non-favourable angular configurations for floating *T. natans* at pseudo-leaf scale led to increasing reflectance in near forward

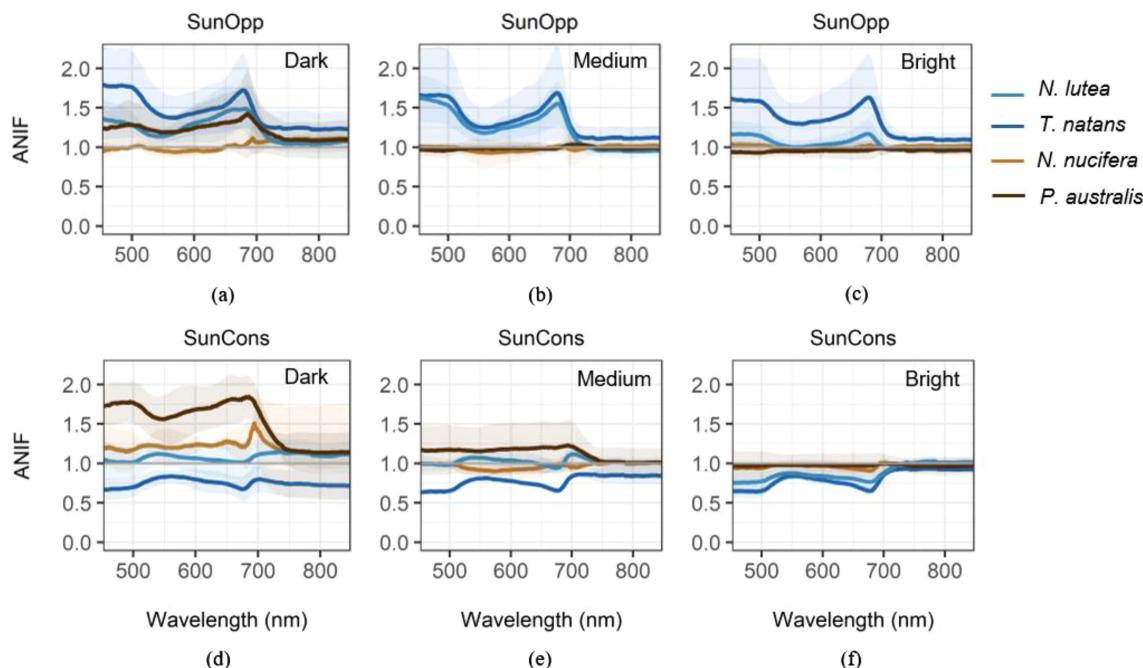


Fig. 6. Mean and standard deviation of ANIF at pseudo-leaf scale for Non-favourable angular configurations plots under viewing directions (a)–(c) opposite SunOpp and (d)–(f) consistent with the sun SunCons, for emergent (*N. nucifera* and *P. australis*) and floating (*N. lutea* and *T. natans*) leaved species. ANIF values are evaluated on different brightness levels (i.e., dark, medium, and bright leaves).

(i.e., SunOpp) direction over all brightness levels [see Fig. 6(a)–(c)]. Off-nadir reflectance of Medium ROIs is around twice the nadir value in Blue and Red ranges, decreasing to 1.25–1.10 in Green and NIR ranges [see Fig. 6(b)]. Such an increment corresponds to a reflectance decrement in SunCons direction, with off-nadir reflectance around 0.60–0.90—the nadir values in the VIS domain [see Fig. 6(e)].

A similar behavior—i.e., reflectance anisotropy increasing in SunOpp direction (more marked for Medium and Dark ROIs)—but attenuated in magnitude is shown by *N. lutea*, which has leaves larger than those of *T. natans* and less prone to surface wetting. Among species with leaves emerging above the water, large-leaved, quasi-planophile *N. nucifera* did not show evident anisotropy patterns even under Non-favourable angular configurations [see Fig. 6(b) and (e)]. The other species, tall riparian helophyte *P. australis*, instead, shows ANIF above unity, in near backward (i.e., SunCons) direction for medium and dark ROIs [about 1.3–1.8; Fig. 6(d) and (e)]. Differently to what shown by floating leaved species, the reflectance increment in SunCons for *P. australis* is not mirrored by an ANIF value lower than 1 in SunOpp direction [see Fig. 6(a) and (b)]. Pseudo-leaf ANIF extracted from plots acquired under favorable angular conditions did not show notable anisotropic effects both in SunCons and SunOpp viewing directions, except for some dark ROIs (see Supplementary Material, Fig. S9).

Fig. 7 describes aquatic vegetation anisotropy at canopy scale, featuring many similarities to pseudo-leaf scale, and some differences. *T. natans* shows an increasing canopy reflectance in SunOpp, peaking around 1.5 ratio in Blue and Red ranges, when  $SZA < 30^\circ$  (Non-favourable configuration), due to the

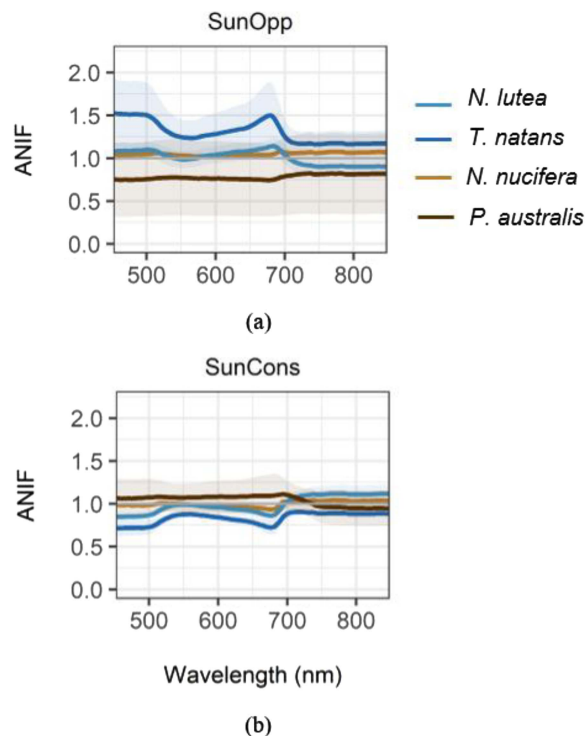


Fig. 7. Mean and standard deviation of ANIF at canopy scale for Non-favourable angular configuration plots under different off-nadir directions (a) opposite with respect to the sun (SunOpp) and (b) consistent with the sun (SunCons), for emergent (*N. nucifera* and *P. australis*) and floating (*N. lutea* and *T. natans*) species.

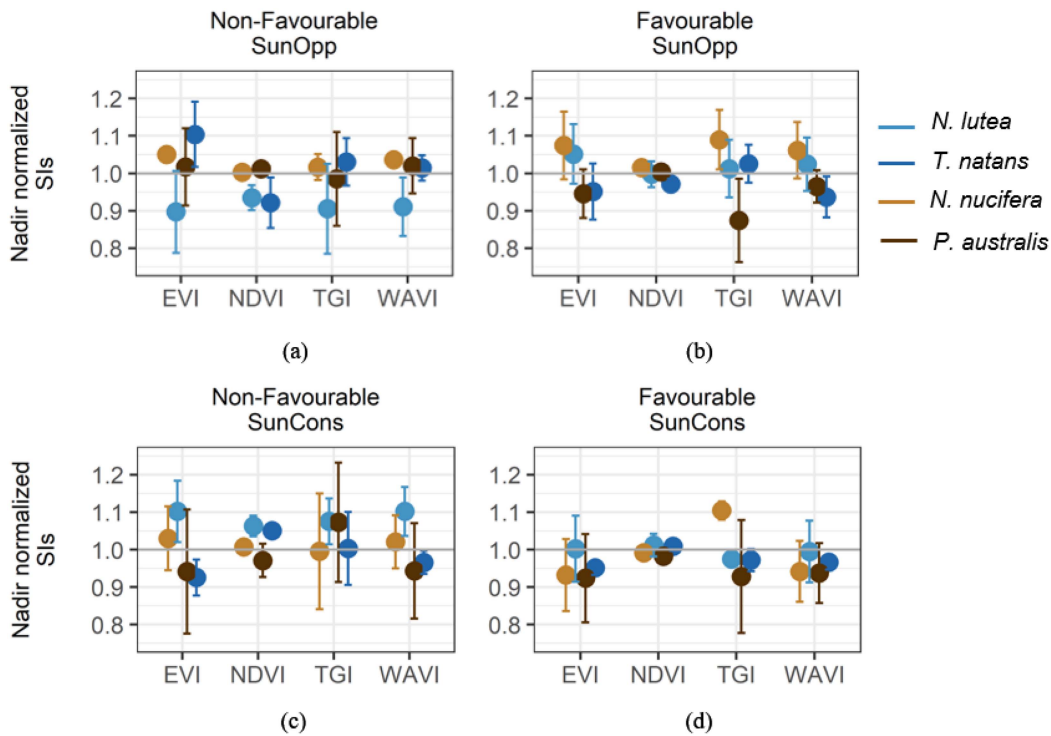


Fig. 8. Mean and standard deviation of nadir-normalized SIs EVI, NDVI, TGI, and WAVI extracted at canopy level under different off-nadir viewing directions, opposite (SunOpp) and consistent (SunCons) with respect to the sun, for (a)–(c) Non-favourable and (b)–(d) favorable angular configurations of both emergent (*N. nucifera* and *P. australis*) and floating (*N. lutea* and *T. natans*) species.

presence of water as canopy background and over some of its floating leaves [see Fig. 7(a)]. This corresponds to a reflectance decrement in SunCons, with ANIF around 0.7 [see Fig. 7(b)]. *N. lutea* shows similar anisotropy patterns, yet attenuated in magnitude. Large, emergent leaves of *N. nucifera*, coupled with relatively high canopy density of this species (i.e., LAI up to 2), make up for very low reflectance anisotropy at canopy scale even under Non-favourable configurations. On the other hand, tall and dense helophyte *P. australis* shows up to 1.15 ANIF value in SunCons, evidencing a backward hotspot effect, mirrored by a consistent decrement in SunOpp, with 0.75 ANIF (especially in the VIS range). Again, no major sign of reflectance anisotropy is highlighted for all the target species when hyperspectral data are acquired under favorable angular configurations (see Supplementary Material, Fig. S10). Furthermore, Supplementary Material (see Figs. S11 and S12) reports average reflectance spectra within SunCons, Nadir, and SunOpp viewing directions at pseudo-leaf and canopy level, respectively.

#### E. Impact of Angular Configurations on Spectral Indices

Mean and standard deviation values for nadir-normalized EVI, NDVI, TGI, and WAVI derived from canopy level ROIs are reported in Fig. 8 per each species, separately for SunOpp and SunCons directions and for favorable and Non-favourable angular configurations. Consistently with patterns shown by spectral reflectance (see Section IV-D), nadir-normalized SIs derived from images acquired under Non-favourable angular configurations are deviating from unity more than those derived

in favorable configurations. This is especially true for floating-leaved species in SunOpp zone [see Fig. 8(a) and (b)] and for species with leaves emerging above water in SunCons zone [see Fig. 8(c) and (d)]. NDVI consistently shows the lowest sensitivity to changes in sun-target-sensor arrangement across all species when acquisitions are performed in favorable angular configuration [see Fig. 8(b) and (d)]. Under Non-favourable configurations, NDVI still manages to attenuate canopy anisotropy for emergent-leaved *N. nucifera* and *P. australis* but WAVI tends to score off-nadir values more similar to nadiral ones over floating-leaved species [see Fig. 8(a) and (c)].

Indeed, the influence of water background spectra on canopy reflectance for the latter species (*N. lutea* and *T. natans*) is more relevant than for the former ones. The effect of angular spectral anisotropy appears more evident on EVI and TGI, varying with the species. EVI relatively attenuates off-nadir distortions better over emergent-leaved than in floating-leaved species under Non-favourable angular configurations [see Fig. 8(a) and (c)]. On the other hand, TGI can attenuate residual anisotropy under favorable configurations over floating-leaved species only [see Fig. 8(b) and (d)].

#### F. Leaf Spectra Similarity Under Different Angular Configurations

Fig. 9 reported SAD with respect to measured leaf spectra of the four aquatic vegetation targets for different angular configurations. Contact spectra and image-derived ones are quite similar to *N. nucifera* due to the big sized, emergent leaves

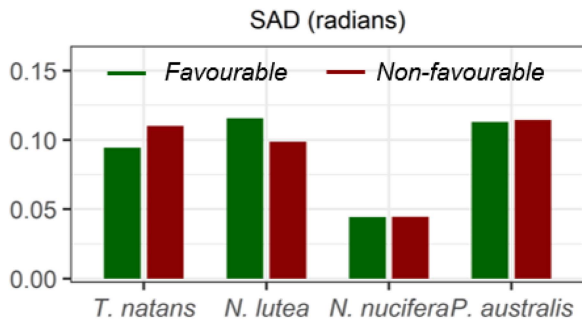


Fig. 9. Spectral similarity evaluation with SAD metric between reference in situ spectra and image-based nadiral pseudo-leaf spectra extracted from hyperspectral cubes, for *T. natans*, *N. lutea*, *N. nucifera*, and *P. australis* aquatic vegetation plots, under favorable and Non-favourable angular configurations.

(SAD = 0.05 rad) that are easy to be delineated at the spatial scale of hyperspectral images. SAD for *P. australis* is higher (around 0.11 rad) than that of *N. nucifera* because pseudo-leaf ROIs for common reed at the imagery resolution are structurally quite different from “pure” leaf targets (e.g., overlapping leaves with variable orientation angles). SAD scores of floating-leaved species are still higher than those of *N. nucifera* since leaf spectra measured in situ on *T. natans* and *N. lutea* were taken after cleaning and wiping the leaves.

SAD for floating-leaved species is slightly different for plots acquired under different angular configurations, i.e., 0.09 and 0.11 rad for *T. natans*, and 0.11 and 0.10 rad for *N. lutea*, respectively, in favorable and Non-favourable conditions.

## V. DISCUSSION

### A. Impact of Illumination Conditions

The presence of water vapor and clouds in the atmosphere determines an increment in diffuse sky irradiance and, generally, less contrasted spatial patterns of surface reflectance due to shadow attenuation. This results in a lower amount of incident radiation reaching the ground, compared to clear sky conditions (with a dominance of solar direct radiation) [51]. In this study, illumination conditions (overcast versus clear sky) were demonstrated to impact on reflectance spectra of floating and emergent aquatic vegetation (see Fig. 3), with an overall decrement in reflectance over the VNIR domain (400–850 nm), more marked at (pseudo)leaf than at canopy scale. Reflectance decrement tends to be stronger in spectrum ranges where vegetation reflectance is higher, i.e., in Green and NIR domains. Relatively few works have quantified the effect of changing light conditions on measured vegetation spectra, focusing exclusively on terrestrial targets [28], [29], [52], and they showed inconsistent results, potentially connected to target anisotropy [14]. Our findings support the call for further empirical studies to be carried out on this topic following the conclusions of Arroyo-Mora et al. [28], even more for usually understudied aquatic vegetation [53].

From our data, illumination conditions effect showed dependence on leaf orientation and distribution. In *N. lutea*, the decrease in VNIR reflectance under overcast sky acquisitions is stronger for floating than emergent leaves; in *P. australis*,

characterized by narrow, aerial leaves with spherical angular distribution, decreasing reflectance is less accentuated in the NIR and more in the VIS range, compared to planophile *N. lutea*. The spectral variability of VNIR reflectance attenuation results into overall lower SIs scores over aquatic vegetation plots when compared with acquisitions under clear sky. This is in line with the findings of [28] but contrasts with those of [52], both based on terrestrial species. Once again, further studies are needed on this topic to extrapolate a clear, generalizable pattern.

Across our target species, NDVI (i.e., Red and NIR reflectance) seems to be less impacted by incoming light variability than other indices (EVI, TGI, and WAVI) that include reflectance in the Blue range, which is more sensitive to atmospheric diffusion than longer wavelengths (Rayleigh scattering). Based on our findings, the use of NDVI as a proxy of the overall amount of photosynthetic material in canopies may contribute to attenuate the effect of incoming light conditions.

On the one hand, the low sensitivity of NDVI to different direct/diffuse incident light ratio was already reported by Ishihara et al. [32] for paddy rice, a crop with periodically flooded canopy background. On the other hand, our results highlight the mentioned pattern for floating-leaved *N. lutea* plots in particular, whereas for emergent canopies of *P. australis* plots, the differences in WAVI, EVI, and TGI between overcast and clear sky acquisitions are less evident (see Fig. 4).

### B. Impact of Angular Configurations

Angular reflectance anisotropy of typical terrestrial vegetation is known to show sensible wavelength dependence. Spectral ranges where reflectance is higher tend to be less anisotropic due to multiple scattering [22], [25], [27], [44]. The overall pattern observed across aquatic vegetation types—showing higher anisotropy in Blue and Red and lower in Green and NIR when scan direction approaches the solar principal plane (see Figs. 6 and 7)—conforms to this behavior both at pseudo-leaf and canopy scales. Radiometric variability due to angular configuration depends on vegetation type, connected to leaf size and predominant orientation, canopy density, structure, and water affinity. Floating and planophile aquatic vegetation (*T. natans* and *N. lutea*) showed the strongest angular sensitivity, mainly depending on SZA. Floating-leaved plots acquired under SZA < 30° show considerable reflectance bias in forward direction (ANIF(SunOpp) > 1) due to water near-specular reflection. This effect is driven by the presence of water drops and a layer on (near-flat) upper leaf surface, and by the plant background (water), respectively, at pseudo-leaf and canopy level. *T. natans* plots are more impacted than those of *N. lutea* because of differences in leaf size and canopy structure. The increase in forward reflectance is mirrored by a decrease in the opposite direction (ANIF(SunCons) < 1). This effect can be explained by gradual dragging of forward hotspot toward nadiral view direction for lower SZA, which results in slightly higher reflectance at nadir than in backward direction, as simulated for aquatic canopies by Zhou et al. [54]. Spectral anisotropy of aquatic vegetation with leaves emerging above the water, represented by *P. australis* and *N. nucifera*, was instead predominantly

driven by the interaction of SZA and RAA. For Non-favourable angular configurations ( $RAA < 30^\circ$ ), our results show evidence of backward hotspot ( $ANIF(\text{SunCons}) > 1$ ) at canopy scale for narrow-leaved, tall *P. australis*. This effect can be attributed to the lower incidence of within-canopy shadows in SunCons than SunOpp direction, consistently with what the literature reports for various terrestrial vegetation types based on models and empirical data [21], [55], [58], [57]. Indeed, among four target species, *P. australis* is the one that most resembles a terrestrial canopy due to its structure and the minor incidence of water background. Specular to floating-leaved vegetation, the increase in backward reflectance is mirrored by a decrease in the opposite direction ( $ANIF(\text{SunOpp}) < 1$ ), which matches the anisotropy behavior delineated by Kimes [17]. At pseudo-leaf scale, results for *P. australis* highlighted a reflectance increment in backward direction [SunCons; Fig. 6(e)], which are not explained by canopy scale mechanisms; we can speculate that leaf orientation for this species (e.g., predominant light backscattering) can be at the basis of such patterns. Since we did not find any detailed quantification of common reed leaf angle distribution, this issue remains open, deserving further investigation. Aquatic vegetation with broad, near flat, and emergent leaves, such as *N. nucifera*, did not show substantial angular distortions at both (pseudo) leaf and canopy scales, possibly due to the limited (yet random) distribution of leaf orientation and canopy heterogeneity. Nevertheless, the fact that Non-favourable angular configurations for *N. nucifera* are represented by very few plots prevents from reaching a conclusion on this point in absence of further investigation.

Published works focusing on terrestrial vegetation have provided evidence that spectral anisotropy exerts an effect on SIs, which depends on vegetation type and canopy structure, beside background influence and sun-sensor geometry [25], [27], [57]. This calls for caution in naively using SIs as proxies of vegetation biophysical features when original data are acquired under variable angular configuration, especially over aquatic vegetation where water presence strongly affects spectral anisotropy [34], [54]. Despite the bias in Red reflectance observed over Non-favourable angular configurations, our results showed relatively moderate or even low anisotropy effects on broadband NDVI. According to our results, the use of NDVI as a proxy of canopy greenness may be less sensitive to anisotropy of aquatic vegetation. This finding is apparently contrasting previous works where NDVI showed significant angular sensitivity in terrestrial vegetation [25], [27], but these authors explored a far wider view angle range than that of our data (maximum range:  $\pm 11^\circ$ ). Background-corrected EVI, a greenness proxy accounting for atmospheric and background interference, was found to be more affected by angular anisotropy than NDVI, with nadir-normalized value sensibly different from unity and high standard deviation in most configurations. This conforms to previously published observations on forest applications, where EVI scored higher angular variability compared to NDVI [57], [58], which were attributed to NIR reflectance saturation in dense canopies. For species with higher water affinity (*T. natans* and, partially, *N. lutea*), the WAVI index, specifically targeted

at surrogating aquatic vegetation canopy density and biomass [49], showed a sensitivity to angular configuration lower or on par with NDVI. Finally, it was TGI, based on VIS spectral bands only and related to vegetation chlorophyll content, the SIs that showed the highest overall sensitivity to angular anisotropy in all species (see Fig. 8).

## VI. CONCLUSION

This work presented a first, empirical-based study on the impact of radiometric variability on centimetric resolution, hyperspectral push-broom imagery acquired from an airborne drone. Two major sources of distortion—illumination (overcast versus clear sky) conditions and angular (sun-target-sensor) configurations—were considered, focusing on aquatic vegetation types that represent different growth forms (floating and emergent species), canopy structure (leaf size, density, and orientation), and connections with water as canopy background. Our results demonstrated an overall lower plant reflectance extracted from hyperspectral images acquired under overcast than clear sky conditions, with stronger incidence in highly reflective bands (e.g., NIR and Green). This effect showed to depend on the observation scale (i.e., more accentuated at pseudo-leaf than at canopy level) and to vary with leaf orientation and distribution, i.e., being more marked for floating plants. Among broadband SIs tested, NDVI tended to be less sensitive to incoming light quality than other indices, including Blue band reflectance (EVI, TGI, and WAVI), over both emergent and floating species. Radiometric variability due to angular configurations showed a strong dependence on aquatic vegetation features (i.e., leaf size and orientation, canopy density and structure, and affinity with water). Indeed, angular anisotropy is mainly driven by SZA (especially lower than  $30^\circ$ ) for floating plants, while it is affected by the interaction of SZA and RAA for plants with leaves emerging above water. Again, NDVI showed lower sensitivity to angular anisotropy compared to EVI and TGI, whereas WAVI scored off-nadir distortions lower or on par with NDVI over plants with floating leaves.

Our preliminary findings highlight the importance of carefully accounting for flight geometry and sun angles as well as actual illumination conditions (diffuse to direct light balance). These factors should be controlled during experimental design and flight planning and execution in order to limit radiometric variability in ultra-high resolution hyperspectral data over aquatic vegetation. In fact, spectroscopy data at centimetric resolution can potentially bring to great advancements in spectro-functional characterization of wetland vegetation at multiple scales, from canopy elements up to individual leaves, provided that radiometric variabilities are controlled and limited. On this point, further works should concentrate on testing a wide range of angular configurations and different illumination conditions, potentially aided by model simulations and by more systematic experiment, possibly controlling for leaf orientation, and on investigating how radiometric variability may impact on reflectance-derived aquatic vegetation features and biophysical-biochemical parameters (e.g., LAI, pigments content).

## ACKNOWLEDGMENT

The authors would like to thank M. Giannoni (IFC-CNR, Italy) for supporting planning and logistics of drone flights. They would also like to thank L. Lastrucci (Natural History Museum of the University of Florence, Italy), M. Cucit (University of Parma, Italy), and M. Comi (Oggiono, Italy) for their help in field activities and data collection. The authors are grateful to Mincio Park authority (Mantua), Natural Reserve “Torbiere del Sebino” (Torbiere), and Natural Reserve “Chiarone” managed by LIPU (Massaciuccoli) for supporting data acquisition and drone overflights in the study areas.

## REFERENCES

- [1] Y. Zhang et al., “Global loss of aquatic vegetation in lakes,” *Earth Sci. Rev.*, vol. 173, pp. 259–265, Oct. 2017, doi: [10.1016/j.earscirev.2017.08.013](https://doi.org/10.1016/j.earscirev.2017.08.013).
- [2] A. Gallant, “The challenges of remote monitoring of wetlands,” *Remote Sens.*, vol. 7, no. 8, pp. 10938–10950, Aug. 2015, doi: [10.3390/rs70810938](https://doi.org/10.3390/rs70810938).
- [3] T. S. F. Silva, M. P. F. Costa, J. M. Melack, and E. M. L. M. Novo, “Remote sensing of aquatic vegetation: Theory and applications,” *Environ. Monit. Assessment*, vol. 140, no. 1–3, pp. 131–145, May 2008, doi: [10.1007/s10661-007-9855-3](https://doi.org/10.1007/s10661-007-9855-3).
- [4] E. Adam, O. Mutanga, and D. Rugege, “Multispectral and hyperspectral remote sensing for identification and mapping of wetland vegetation: A review,” *Wetlands Ecol. Manage.*, vol. 18, no. 3, pp. 281–296, Jun. 2010, doi: [10.1007/s11273-009-9169-z](https://doi.org/10.1007/s11273-009-9169-z).
- [5] M. Guo, J. Li, C. Sheng, J. Xu, and L. Wu, “A review of wetland remote sensing,” *Sensors*, vol. 17, no. 4, Apr. 2017, Art. no. 777, doi: [10.3390/s17040777](https://doi.org/10.3390/s17040777).
- [6] P. S. Thenkabail and J. G. Lyon, *Hyperspectral Remote Sensing of Vegetation*. Boca Raton, FL, USA: CRC, 2016, doi: [10.1201/b11222](https://doi.org/10.1201/b11222).
- [7] J. Verrelst et al., “Quantifying vegetation biophysical variables from imaging spectroscopy data: A review on retrieval methods,” *Surv. Geophys.*, vol. 40, no. 3, pp. 589–629, May 2019, doi: [10.1007/s10712-018-9478-y](https://doi.org/10.1007/s10712-018-9478-y).
- [8] T. B. Hank et al., “Spaceborne imaging spectroscopy for sustainable agriculture: Contributions and challenges,” *Surv. Geophys.*, vol. 40, no. 3, pp. 515–551, May 2019, doi: [10.1007/s10712-018-9492-0](https://doi.org/10.1007/s10712-018-9492-0).
- [9] S. Khanna, M. J. Santos, S. L. Ustin, and P. J. Haverkamp, “An integrated approach to a biophysically based classification of floating aquatic macrophytes,” *Int. J. Remote Sens.*, vol. 32, no. 4, pp. 1067–1094, Feb. 2011, doi: [10.1080/014311609035505328](https://doi.org/10.1080/014311609035505328).
- [10] D. Stratoulas, H. Balzter, A. Zlinszky, and V. R. Tóth, “A comparison of airborne hyperspectral-based classifications of emergent wetland vegetation at lake Balaton, Hungary,” *Int. J. Remote Sens.*, vol. 39, no. 17, pp. 5689–5715, Sep. 2018, doi: [10.1080/01431161.2018.1466081](https://doi.org/10.1080/01431161.2018.1466081).
- [11] P. Villa, M. Pinardi, V. R. Tóth, P. D. Hunter, R. Bolpagni, and M. Bresciani, “Remote sensing of macrophyte morphological traits: Implications for the management of shallow lakes,” *J. Limnol.*, vol. 76, Mar. 2017, Art. no. s1, doi: [10.4081/jlimnol.2017.1629](https://doi.org/10.4081/jlimnol.2017.1629).
- [12] H. Aasen and A. Bolten, “Multi-temporal high-resolution imaging spectroscopy with hyperspectral 2D imagers – From theory to application,” *Remote Sens. Environ.*, vol. 205, pp. 374–389, Feb. 2018, doi: [10.1016/j.rse.2017.10.043](https://doi.org/10.1016/j.rse.2017.10.043).
- [13] J. Jeziorska, “UAS for wetland mapping and hydrological modeling,” *Remote Sens.*, vol. 11, no. 17, Aug. 2019, Art. no. 1997, doi: [10.3390/rs11171997](https://doi.org/10.3390/rs11171997).
- [14] A. Damm, L. Guanter, W. Verhoef, D. Schlöpfer, S. Garbari, and M. E. Schaepman, “Impact of varying irradiance on vegetation indices and chlorophyll fluorescence derived from spectroscopy data,” *Remote Sens. Environ.*, vol. 156, pp. 202–215, Jan. 2015, doi: [10.1016/j.rse.2014.09.031](https://doi.org/10.1016/j.rse.2014.09.031).
- [15] J. Weyermann, *Reflectance Anisotropy Effects in Optical Remote Sensing Data*. Zürich, Switzerland: Univ. Zurich, 2016.
- [16] F. E. Nicodemus, *Geometrical Considerations and Nomenclature For Reflectance*, vol. 160. Washington, DC, USA: National Bureau Standard, 1977.
- [17] D. S. Kimes, “Radiative transfer in homogeneous and heterogeneous vegetation canopies,” in *Proc. Photon-Vegetation Interact.*, 1991, pp. 339–388, doi: [10.1007/978-3-642-75389-3\\_11](https://doi.org/10.1007/978-3-642-75389-3_11).
- [18] X. Li and A. H. Strahler, X. Li, and A. H. Strahler, “Geometric-optical bidirectional reflectance modeling of the discrete crown vegetation canopy: Effect of crown shape and mutual shadowing,” *IEEE Trans. Geosci. Remote Sens.*, vol. 30, no. 2, pp. 276–292, Mar. 1992.
- [19] H. Breece and R. Holmes, “Bidirectional scattering characteristics of healthy green soybean and corn leaves in vivo,” *Appl. Opt.*, vol. 10, pp. 119–127, 1971.
- [20] D. Biliouris, W. Verstraeten, P. Dutré, J. van Aardt, B. Muys, and P. Coppin, “A compact laboratory spectro-goniometer (CLabSpeG) to assess the BRDF of materials. Presentation, calibration and implementation on *Fagus sylvatica* L. Leaves,” *Sensors*, vol. 7, no. 9, pp. 1846–1870, Sep. 2007, doi: [10.3390/s7091846](https://doi.org/10.3390/s7091846).
- [21] D. S. Kimes, “Dynamics of directional reflectance factor distributions for vegetation canopies,” *Appl. Opt.*, vol. 22, no. 9, May 1983, Art. no. 1364, doi: [10.1364/AO.22.001364](https://doi.org/10.1364/AO.22.001364).
- [22] S. R. Sandmeier and K. I. Itten, “A field goniometer system (FI-GOS) for acquisition of hyperspectral BRDF data,” *IEEE Trans. Geosci. Remote Sens.*, vol. 37, no. 2, pp. 978–986, Mar. 1999, doi: [10.1109/36.752216](https://doi.org/10.1109/36.752216).
- [23] A. Burkart, H. Aasen, L. Alonso, G. Menz, G. Bareth, and U. Rascher, “Angular dependency of hyperspectral measurements over wheat characterized by a novel UAV based goniometer,” *Remote Sens.*, vol. 7, no. 1, pp. 725–746, Jan. 2015, doi: [10.3390/rs70100725](https://doi.org/10.3390/rs70100725).
- [24] M. Danner, K. Berger, M. Wocho, W. Mauter, and T. Hank, “Retrieval of biophysical crop variables from multi-angular canopy spectroscopy,” *Remote Sens.*, vol. 9, no. 7, Jul. 2017, Art. no. 726, doi: [10.3390/rs9070726](https://doi.org/10.3390/rs9070726).
- [25] L. S. Galvão, F. J. Ponzoni, J. C. N. Epiphanyo, B. F. T. Rudorff, and A. R. Formaggio, “Sun and view angle effects on NDVI determination of land cover types in the Brazilian Amazon region with hyperspectral data,” *Int. J. Remote Sens.*, vol. 25, no. 10, pp. 1861–1879, May 2004, doi: [10.1080/01431160310001598908](https://doi.org/10.1080/01431160310001598908).
- [26] P. Roosjen, J. Suomalainen, H. Bartholomeus, and J. Clevers, “Hyperspectral reflectance anisotropy measurements using a pushbroom spectrometer on an unmanned aerial vehicle—Results for barley, winter wheat, and potato,” *Remote Sens.*, vol. 8, no. 11, Nov. 2016, Art. no. 909, doi: [10.3390/rs8110909](https://doi.org/10.3390/rs8110909).
- [27] J. Verrelst, M. E. Schaepman, B. Koetz, and M. Kneubühler, “Angular sensitivity analysis of vegetation indices derived from CHRIS/PROBA data,” *Remote Sens. Environ.*, vol. 112, no. 5, pp. 2341–2353, May 2008, doi: [10.1016/j.rse.2007.11.001](https://doi.org/10.1016/j.rse.2007.11.001).
- [28] J. P. Arroyo-Mora et al., “Assessing the impact of illumination on UAV pushbroom hyperspectral imagery collected under various cloud cover conditions,” *Remote Sens. Environ.*, vol. 258, Jun. 2021, Art. no. 112396, doi: [10.1016/j.rse.2021.112396](https://doi.org/10.1016/j.rse.2021.112396).
- [29] M. Shoshany, H. Spond, and D. E. Bar, “Overcast versus clear-sky remote sensing: Comparing surface reflectance estimates,” *Int. J. Remote Sens.*, vol. 40, no. 17, pp. 6737–6751, Sep. 2019, doi: [10.1080/01431161.2019.1591649](https://doi.org/10.1080/01431161.2019.1591649).
- [30] A. Kuusk, “Monitoring of vegetation parameters on large areas by the inversion of a canopy reflectance model,” *Int. J. Remote Sens.*, vol. 19, no. 15, pp. 2893–2905, Jan. 1998, doi: [10.1080/014311698214334](https://doi.org/10.1080/014311698214334).
- [31] V. C. Vanderbilt et al., “Inundation discriminated using sun glint,” *IEEE Trans. Geosci. Remote Sens.*, vol. 40, no. 6, pp. 1279–1287, Jun. 2002, doi: [10.1109/TGRS.2002.800233](https://doi.org/10.1109/TGRS.2002.800233).
- [32] M. Ishihara, Y. Inoue, K. Ono, M. Shimizu, and S. Matsuura, “The impact of sunlight conditions on the consistency of vegetation indices in croplands—Effective usage of vegetation indices from continuous ground-based spectral measurements,” *Remote Sens.*, vol. 7, no. 10, pp. 14079–14098, Oct. 2015, doi: [10.3390/rs71014079](https://doi.org/10.3390/rs71014079).
- [33] A. Kuusk, “The hot spot effect in plant canopy reflectance,” in *Proc. Photon-Vegetation Interact.*, 1991, pp. 139–159, doi: [10.1007/978-3-642-75389-3\\_5](https://doi.org/10.1007/978-3-642-75389-3_5).
- [34] G. Zhou, C. Niu, W. Xu, W. Yang, J. Wang, and H. Zhao, “Canopy modeling of aquatic vegetation: A radiative transfer approach,” *Remote Sens. Environ.*, vol. 163, pp. 186–205, Jun. 2015, doi: [10.1016/j.rse.2015.03.015](https://doi.org/10.1016/j.rse.2015.03.015).
- [35] F. Eller et al., “Cosmopolitan species as models for ecophysiological responses to global change: The common reed *Phragmites australis*,” *Front. Plant Sci.*, vol. 8, Nov. 2017, Art. no. 01833, doi: [10.3389/fpls.2017.01833](https://doi.org/10.3389/fpls.2017.01833).
- [36] M. Marks, B. Lapin, and J. Randall, “*Phragmites australis* (P. Communis): Threats, management, and monitoring,” *Nature*, vol. 14, pp. 285–229, 1994.

- [37] B. Poulin, A. Davranche, and G. Lefebvre, "Ecological assessment of Phragmites australis wetlands using multi-season SPOT-5 scenes," *Remote Sens. Environ.*, vol. 114, no. 7, pp. 1602–1609, Jul. 2010, doi: [10.1016/j.rse.2010.02.014](https://doi.org/10.1016/j.rse.2010.02.014).
- [38] V. R. Tóth, P. Villa, M. Pinardi, and M. Bresciani, "Aspects of invasiveness of Ludwigia and Nelumbo in shallow temperate fluvial lakes," *Front. Plant Sci.*, vol. 10, May 2019, Art. no. 01833, doi: [10.3389/fpls.2019.00647](https://doi.org/10.3389/fpls.2019.00647).
- [39] P. Villa et al., "Assessing macrophyte seasonal dynamics using dense time series of medium resolution satellite data," *Remote Sens. Environ.*, vol. 216, pp. 230–244, Oct. 2018, doi: [10.1016/j.rse.2018.06.048](https://doi.org/10.1016/j.rse.2018.06.048).
- [40] A. M. Chernova, "Non-destructive estimation of the leaf area in Nuphar Lutea L. Nymphaeaceae," *Mod. Phytomorphol.*, vol. 9, pp. 13–20, 2019.
- [41] S. S. Phartyal, S. Rosbakh, and P. Poschlo, "Seed germination ecology in *Trapa natans* L., a widely distributed freshwater macrophyte," *Aquatic Botany*, vol. 147, pp. 18–23, Jun. 2018, doi: [10.1016/j.aquabot.2018.02.001](https://doi.org/10.1016/j.aquabot.2018.02.001).
- [42] R. E. Bird and C. Riordan, "Simple solar spectral model for direct and diffuse irradiance on horizontal and tilted planes at the earth's surface for cloudless atmospheres," *J. Appl. Climatol.*, vol. 25, no. 1, pp. 87–97, Jan. 1986, doi: [10.1175/1520-0450\(1986\)025<0087:SSSMFD>2.0.CO;2](https://doi.org/10.1175/1520-0450(1986)025<0087:SSSMFD>2.0.CO;2).
- [43] A. Savitzky and M. J. Golay, "Smoothing and differentiation of data by simplified least squares procedures," *Anal. Chem.*, vol. 36, pp. 1627–1639, 1964.
- [44] S. Sandmeier, C. Müller, B. Hosgood, and G. Andreoli, "Physical mechanisms in hyperspectral BRDF data of grass and water-cress," *Remote Sens. Environ.*, vol. 66, no. 2, pp. 222–233, Nov. 1998, doi: [10.1016/S0034-4257\(98\)00060-1](https://doi.org/10.1016/S0034-4257(98)00060-1).
- [45] J. W. Rouse, R. H. Haas, J. A. Schell, and D. W. Deering, "Monitoring vegetation systems in the great plains with ERTS," in *Proc. 3rd ERTS-1 Symp. NASA*, 1974, pp. 309–317.
- [46] A. Huete, "A comparison of vegetation indices over a global set of TM images for EOS-MODIS," *Remote Sens. Environ.*, vol. 59, no. 3, pp. 440–451, Mar. 1997, doi: [10.1016/S0034-4257\(96\)00112-5](https://doi.org/10.1016/S0034-4257(96)00112-5).
- [47] B. Matsushita, W. Yang, J. Chen, Y. Onda, and G. Qiu, "Sensitivity of the enhanced vegetation index (EVI) and normalized difference vegetation index (NDVI) to topographic effects: A case study in high-density cypress forest," *Sensors*, vol. 7, no. 11, pp. 2636–2651, Nov. 2007, doi: [10.3390/s7112636](https://doi.org/10.3390/s7112636).
- [48] E. R. Hunt, C. S. T. Daughtry, J. U. H. Eitel, and D. S. Long, "Remote sensing leaf chlorophyll content using a visible band index," *Agron. J.*, vol. 103, no. 4, pp. 1090–1099, Jul. 2011, doi: [10.2134/agronj2010.0395](https://doi.org/10.2134/agronj2010.0395).
- [49] P. Villa, A. Mousivand, and M. Bresciani, "Aquatic vegetation indices assessment through radiative transfer modeling and linear mixture simulation," *Int. J. Appl. Earth Observation Geoinf.*, vol. 30, pp. 113–127, Aug. 2014, doi: [10.1016/j.jag.2014.01.017](https://doi.org/10.1016/j.jag.2014.01.017).
- [50] F. A. Kruse et al., "The spectral image processing system (SIPS)—Interactive visualization and analysis of imaging spectrometer data," *Remote Sens. Environ.*, vol. 44, no. 2–3, pp. 145–163, May 1993, doi: [10.1016/0034-4257\(93\)90013-N](https://doi.org/10.1016/0034-4257(93)90013-N).
- [51] A. P. Brunger and F. C. Hooper, "Anisotropic sky radiance model based on narrow field of view measurements of shortwave radiance," *J. Sol. Energy*, vol. 51, no. 1, pp. 53–64, Jul. 1993, doi: [10.1016/0038-092X\(93\)90042-M](https://doi.org/10.1016/0038-092X(93)90042-M).
- [52] R. de Souza, C. Buchhart, K. Heil, J. Plass, F. M. Padilla, and U. Schmidhalter, "Effect of time of day and sky conditions on different vegetation indices calculated from active and passive sensors and images taken from UAV," *Remote Sens.*, vol. 13, no. 9, Apr. 2021, Art. no. 1691, doi: [10.3390/rs13091691](https://doi.org/10.3390/rs13091691).
- [53] P. Villa, R. Bolpagni, M. Pinardi, and V. R. Tóth, "Leaf reflectance can surrogate foliar economics better than physiological traits across macrophyte species," *Plant Methods*, vol. 17, no. 1, Dec. 2021, Art. no. 115, doi: [10.1186/s13007-021-00816-4](https://doi.org/10.1186/s13007-021-00816-4).
- [54] G. Zhou, S. Yang, S. Sathyendranath, and T. Platt, "Canopy modeling of aquatic vegetation: A geometric optical approach (AVGO)," *Remote Sens. Environ.*, vol. 245, Aug. 2020, Art. no. 111829, doi: [10.1016/j.rse.2020.111829](https://doi.org/10.1016/j.rse.2020.111829).
- [55] D. W. Deering, E. M. Middleton, and T. F. Eck, "Reflectance anisotropy for a spruce-hemlock forest canopy," *Remote Sens. Environ.*, vol. 47, no. 2, pp. 242–260, Feb. 1994, doi: [10.1016/0034-4257\(94\)90159-7](https://doi.org/10.1016/0034-4257(94)90159-7).
- [56] J. R. Irons, K. J. Ranson, D. L. Williams, R. R. Irish, and F. G. Huegel, "An off-nadir-pointing imaging spectroradiometer for terrestrial ecosystem studies," *IEEE Trans. Geosci. Remote Sens.*, vol. 29, no. 1, pp. 66–74, Jan. 1991, doi: [10.1109/36.103294](https://doi.org/10.1109/36.103294).
- [57] L. S. Galvão, F. M. Breunig, J. R. dos Santos, and Y. M. de Moura, "View-illumination effects on hyperspectral vegetation indices in the Amazonian tropical forest," *Int. J. Appl. Earth Observation Geoinf.*, vol. 21, pp. 291–300, Apr. 2013, doi: [10.1016/j.jag.2012.07.005](https://doi.org/10.1016/j.jag.2012.07.005).
- [58] D. A. Sims, A. F. Rahman, E. F. Vermote, and Z. Jiang, "Seasonal and inter-annual variation in view angle effects on MODIS vegetation indices at three forest sites," *Remote Sens. Environ.*, vol. 115, no. 12, pp. 3112–3120, Dec. 2011, doi: [10.1016/j.rse.2011.06.018](https://doi.org/10.1016/j.rse.2011.06.018).



**Erika Piaser** received the master's degree in environmental and land planning engineering in 2020 from Politecnico di Milano, Milan, Italy, where she is currently working toward the 37th cycle Ph.D. degree in environmental and infrastructure engineering (geodesy and geomatics area).

She is currently a Research Fellow with the Institute for Electromagnetic Sensing of the Environment, National Research Council of Italy, Milan, Italy. Her research specifically focused on remote sensing and in situ applications for aquatic vegetation monitoring and mapping.



**Andrea Bertoni** received the bachelor degree in biomedical engineering from the University of Pisa, Pisa, Italy, in 2007.

He is with the Institute of Geosciences and Earth Resources, National Research Council (IGG-CNR), Pisa, Italy. He is the Head of the additional service "REMOTE" of the CNR Area in Pisa, which supports researchers and companies by offering a service of design, implementation, and management of tools useful for remote sensing investigations and purposes, mainly with UAV platforms.



**Rossano Bolpagni** received the M.Sc. (*Laurea*) degree in biology in 2000 and the Ph.D. degree in ecology in 2006, both from the University of Parma, Parma, Italy.

He works with the Aquatic Ecology unit of the Department of Chemistry, Life Sciences and Environmental Sustainability, Parma University, and has been collaborating with the IREA-CNR since 2008. He is a member of the Editorial Board for *Aquatic Botany* and the *Journal of Limnology* on the topics of macrophytes. His research interests focus on inland waters and wetland ecosystems, with special emphasis on aquatic primary producers. His research embraces interdisciplinary, comparative, and contextual approaches aimed at investigating the environmental determinants of aquatic biodiversity and its responses to human mediated impacts. A particular effort is devoted to applying functional methods to study macrophytes.



**Michele Caccia** received the master's degree in physics from the University of Milan, Milan, Italy, in 2003, and the Ph.D. degree in physics and astronomy from the University Milano-Bicocca, Milan, Italy, in 2007.

He is currently operating within the Institute of Molecular Bioimaging and Physiology of the National Research Council (IBFM-CNR), Milan, as a Researcher on computer science and data processing. His main research interests focus on the analysis of multi- and hyperspectral images in the visible, infrared, and X-rays to investigate the physicochemical properties of different types of samples. His research finds application in a wide scenario that spans from in vivo cell dynamic and tumorigenesis to the characterization and conservation of any kind of cultural heritage artefact, such as paintings or sculptures.



**Maria Beatrice Castellani** received the M.Sc. (*Laurea*) degree in conservation and management of nature from the University of Florence, Florence, Italy, in 2018 and the Ph.D. degree in evolutionary biology and ecology from the University of Parma, Parma, Italy, in 2023.

She worked with the Centre for Ecology, Evolution and Environmental Changes, University of Lisbon, in 2019. To date, she is a Research Fellow with the Biology Department of the University of Florence, Florence. Her research interests focus on the study of the genetic diversity of freshwater macrophyte at both local and regional scales from the population to community level, in particular, to relate genetic diversity data with those of spectro-functional diversity and to decipher the adaptive processes shaping the evolution of focal species dominating Italian wetlands.



**Francesca Gallivanone** received the master's degree in physics (specialization in health physics) from the University of Milan, Milan, Italy, in 2007, and the Ph.D. degree in biomedical technologies from the University of Milan-Bicocca, Milan, in 2010.

She has been a Researcher with IBFM-CNR, Milan, since 2011 within the Laboratory of Innovation and Integration in Molecular Medicine. She was the Project Manager of the European project "DECIDE: Diagnostic Enhancement of Confidence by an International Distributed Environment," funded by the European Commission within the FP7 Program. Her research activities are focused on the development of innovative methods and applications based on analytical-experimental, statistical, and integrated approaches for the extraction and quantification of imaging and signal biomarkers both at preclinical and clinical levels.



**Andrea Coppi** received the master's degree in natural science in 2004 and the Ph.D. degree in biosystematics and plant ecology in 2008, both from the University of Florence, Florence, Italy.

Since 2022, he has been an Associate Professor with the Department of Biology, University of Florence, where he also coordinates the Laboratory of Environmental and Applied Botany. He has been a Lecturer in courses since 2015 in plant biodiversity, forensic botany, reproductive strategies, and the evolution of plants. He is the supervisor of about 30 university theses (bachelor's, master's, and Ph.D. degrees). He is an Associate Editor for *Caryologia: International Journal of Cytology, Cytosystematics and Cytogenetics* (Taylor and Francis), and for the journal *Frontiers in Evolutionary and Population Genetics*. His research activities cover the field of biosystematics and plant ecology. The research focuses on using specific molecular (DNA-based) approaches in studies regarding phylogenetic systematics, population genetics, biogeography, and the conservation status of plant species.



**Giovanna Sona** received the degree in physics with honors from the University of Milan, Milan, Italy, in 1987 and the Ph.D. degree in geodetic and topographic science from Politecnico di Milano, Milan, Italy, in 1994.

She was an Analyst of environmental data (numerical methods for the identification of pollutant sources), then a Reservoir Modelist in Oil company Agip S.p.A., testing and applying numerical models for gas and oil flows in porous media. She is currently a Researcher with Politecnico di Milano, where she works in the fields of photogrammetry, remote sensing, and image analysis. She follows the development and use of vector/sensor unmanned systems (UAS) for environmental surveys and proximal sensing and the analysis of UAS multi-spectral and thermal images to assess their geometric and radiometric quality, and their use in photogrammetric 3-D modeling, with a focus on vegetation studies and precision agriculture. She is a Professor for bachelor's and master's courses, for the courses of GIS applications, topography and cartography, digital photogrammetry, remote sensing, and digital image analysis.



**Alice Dalla Vecchia** received the M.Sc. (*Laurea*) degree in ecology and nature conservation from the University of Parma, Parma, Italy, in 2019. She is currently working toward the Ph.D. degree in evolutionary biology and ecology, to be obtained in 2023, with the University of Parma, Parma, Italy.

She worked with the Laboratory of Aquatic Ecology, University of Parma, and has been an Associate Researcher at IREA-CNR since 2019. Her research interests focus on macrophytes environmental interactions, macrophytes resource-use strategies, and functional traits plasticity. Her research has so far covered different groups of macrophytes, from submerged to emergent, but focusing on rooted floating and free-floating species, and how environmental conditions affect traits plasticity. Other topics of research include the implementation of protocols for traits measures on critical macrophytes groups, the investigation of community structure along a gradient of disturbance, and the contribution of invasive species to macrophytes and riparian communities.



**Paolo Villa** received the M.Sc. (*Laurea*) degree in environmental engineering in 2004 and the Ph.D. degree in geomatics in 2008, both from the Polytechnic University of Milan, Milano, Italy.

He was with Remote Sensing Laboratory, Polytechnic of Milan, and has been a Researcher with the Institute for Electromagnetic Sensing of the Environment, CNR, Milan, Italy, since 2012. He is a member of the Editorial Board for the *International Journal of Applied Earth Observation and Geoinformation* and for *Wetlands Ecology and Management* on the topics of remote sensing and GIS. His research interests focus on multi- and hyperspectral image processing, aimed at monitoring environmental phenomena dynamics at different scales through Earth Observation. His research covers heterogeneous applications, dealing with land cover change, agriculture, aquatic ecosystem, plant community diversity, soil sealing, geology, and natural hazards.

Open Access funding provided by 'Consiglio Nazionale delle Ricerche-CARI-CARE-ITALY' within the CRUI CARE Agreement